

Development of a Characteristic-Based Finite Volume Method for Patch Antennas¹

Dr. Jeffrey L. Young, Principal Investigator
Department of Electrical Engineering
MRC Institute
University of Idaho

October 1999

¹Final report for DEPSCoR grant F49620-96-1-0469. Monitored by Dr. Arje Nachman of the AFOSR.

REPORT DOCUMENTATION PAGE

AFRL-SR-BL-TR-00-

Public reporting burden for this collection of information is estimated to average 1 hour per response, including the time for reviewing this collection of information. Send comments regarding this burden estimate or any other aspect of this collection of information, including suggestions for reducing this burden to Washington Headquarters Services, Directorate for Information Operations and Reports, 1215 Jefferson Davis Highway, Suite 1204, Arlington, VA 22202-4302, and to the Office of Management and Budget, Paperwork Reduction Project (0704-0188), Washington, DC 20503

g and maintaining
suggestions for
d to the Office of

1. AGENCY USE ONLY (Leave blank)		2. REPORT DATE 14- Oct -1999	3. REPORT TYPE AND DATES COVERED Final 15-Sept-1996 - 14-Sept-1999	
4. TITLE AND SUBTITLE Development of a Characteristic-Based Finite Volume Method for Patch Antennas			5. FUNDING NUMBERS G F49620-96-1-0469 PR-TA 3484/BS	
6. AUTHOR(S) Jeffrey L. Young Associate Professor of Electrical Engineering				
7. PERFORMING ORGANIZATION NAME(S) AND ADDRESS(ES) University of Idaho Grants and Contracts Office Room 213 Admin Office Building Moscow, ID 83844-3142			8. PERFORMING ORGANIZATION REPORT NUMBER 96074	
9. SPONSORING / MONITORING AGENCY NAME(S) AND ADDRESS(ES) AFOSR/NM Room 723 801 North Randolph Street Arlington, VA 22203-1977			10. SPONSORING / MONITORING AGENCY REPORT NUMBER	
11. SUPPLEMENTARY NOTES				
12a. DISTRIBUTION / AVAILABILITY STATEMENT DISTRIBUTION STATEMENT A Approved for Public Release Distribution Unlimited				12b. DISTRIBUTION CODE
13. ABSTRACT (Maximum 200 Words) An overview of the work accomplished throughout the duration of the contract is contained herein. This overview is cast primarily in terms of measurable accomplishments (i.e., publications and numerical solvers) and challenges (technical and non-technical). With respect to the former, five manuscripts have been accepted for or submitted to refereed journals, four manuscripts were presented at technical conferences, two manuscripts were co-authored with AFRL personnel, and one manuscript was invited for publication by the IEEE Trans. on Antennas and Propagation. Additionally, five numerical solvers have been developed and extensively tested. Representative data associated with each of these solvers are provided to corroborate the numerical methodology with the expected outcomes. Additional information pertaining to graduate student involvement, interactions with AFRL personnel, facilities and future work is also provided. Attached as appendices to the report are specific technical details associated with two numerical solvers hitherto not published in the open literature.				
14. SUBJECT TERMS Numerical Methods, Finite-Volume, Electromagnetics				15. NUMBER OF PAGES 44
				16. PRICE CODE
17. SECURITY CLASSIFICATION OF REPORT Unclassified	18. SECURITY CLASSIFICATION OF THIS PAGE Unclassified	19. SECURITY CLASSIFICATION OF ABSTRACT Unclassified	20. LIMITATION OF ABSTRACT UL	

NSN 7540-01-280-5500

Standard Form 298 (Rev. 2-89)
Prescribed by ANSI Std. Z39-18
298-102

DTIC QUALITY INSPECTED 4

Contents

1	Executive Summary	2
2	Measurable Accomplishments	3
2.1	Publications	3
2.2	Numerical Solvers	4
2.2.1	3WB1–RK4 FVTD Solver	4
2.2.2	D4–RK4 FDTD Solver	13
2.2.3	CC4–RK4 Solver	15
2.2.4	C4–LF4 Solver	16
2.2.5	Yee FDTD Solver	18
3	Challenges	20
3.1	Non–Technical Challenges	20
3.2	3WB1–RK4 FVTD Solver: Technical Challenges	20
3.3	D4–RK4 Solver: Technical Challenges	21
3.4	CC4–RK4 Solver: Technical Challenges	22
3.5	C4–LF4 Solver: Technical Challenges	22
3.6	Yee FDTD Solver: Technical Challenges	22
4	Graduate Students	23
5	Interactions with AFRL Personnel	23
6	Facilities	23
7	Web Page	24
8	Future Work	24
9	Acknowledgements	24
A	Appendix: Finite–Volume Procedure	26
B	Appendix: High–Order Leap–Frog Integrator	35

1 Executive Summary

With funding from the Defense Experimental Program to Stimulate Competitive Research (DEPSCoR), the Laboratory of Applied Computational Electromagnetics was created within the MRC Institute at the University of Idaho. The purpose of this funding, as stated in the proposal "Development of a Characteristic-Based, Finite-Volume Method for Patch Antennas," was to conduct research in the development and test of time-domain algorithms for Maxwell's equations. Specifically, the main objectives of this research endeavor are as follows:

1. To develop finite-volume numerical codes for the square, circular and elliptical patch antennas.
2. To determine the optimal grid and grid density for these geometries.
3. To develop appropriate feed models so that input impedance data can be ascertained.
4. To incorporate higher-order algorithms as they are being developed and tested at the Flight Dynamics Directorate, WPAFB.
5. To investigate the use of finite-difference schemes on a general curvilinear frame.
6. To numerically compute the effects of finite-size ground planes and superstrate dielectrics on the radiation and impedance characteristics of the antennas.
7. To publish research results in archival, peer-reviewed journals.

As described herein, most of these objectives have been fully or partially satisfied. Specifically, the following accomplishments have been realized:

1. A curvilinear, three-dimensional, finite-volume, time-domain solver has been built, extensively tested and applied to the patch antenna problem.
2. Analytical studies on the effect of grid density on solution accuracy have been conducted.
3. Several different feed models have been devised and tested for the excitation of the patch antenna.
4. A dedicated effort in devising and coding stable, high-order finite-difference schemes has been applied.
5. Numerous papers have been submitted to, accepted by or printed in international refereed journals and/or conferences.

Note: Objective five has not been satisfied. Our finite-difference solver is still being developed for Cartesian-based grids. As for objective six, the finite-volume code is capable of conducting the stated objective; the numerical investigation was not completed.

2 Measurable Accomplishments

Tangible productivity metrics of the Principal Investigator's (PI) team are defined by publication output and code development activities.

2.1 Publications

The following manuscripts were submitted to or published in peer-reviewed, refereed journals during the course of this contract:

- 1 J. F. Nystrom and J. L. Young, "k-space transfer function design of discrete operators: Application to Maxwell's time-domain equations," *Journal of Electromagnetic Waves & Applications*, vol. 13, pp. 781-806, 1999.
- 2 J. L. Young, "The design of high-order, leap-frog integrators for Maxwell's equations," *IEEE Trans. Antennas & Propagation* (Submitted).
- 3 J. F. Nystrom, "High-order, time-stable numerical boundary condition scheme for the temporally dependent Maxwell equations in two-dimensions", *Journal of Computational Physics* (Submitted).
- 4 J. L. Young, R. Nelson and D. V. Gaitonde, "A Detailed examination of the finite-volume, time-domain method for Maxwell's equations." *Journal of Electromagnetic Waves & Applications* (Submitted).

The following manuscripts were presented at international conferences:

- 5 J. F. Nystrom and J. L. Young, "k-space transfer function design of discrete operators: Application to Maxwell's time-domain equations," *37th AIAA Aerospace Science Meeting and Exhibit*, AIAA 99-337, Reno, NV, 1999.
- 6 J. L. Young, "The design of high-order leap-frog integrators for Maxwell's equations," *IEEE Antennas and Propagation International Symposium and USNC/URSI National Radio Science Meeting*, Orlando, FL., pp. 176-179, 1999.
- 7 J. F. Nystrom and J. L. Young, "High-order, finite-difference procedure for the temporally dependent Maxwell's equations," *IEEE Antennas and Propagation International Symposium and USNC/URSI National Radio Science Meeting*, Atlanta, GA., 1998.
- 8 J. L. Young and J. F. Nystrom, "Designing high-order, time-domain numerical solvers for Maxwell's equations," *IEEE Antennas and Propagation International Symposium and USNC/URSI National Radio Science Meeting*, Atlanta, GA., pp. 546-549, 1998.

The following papers resulted from a joint research collaboration between the PI and the scientists in the Air Force Research Laboratory (also see item 4):

- 9 D. Gaitonde, J. Shang and J. L. Young, "Practical aspects of higher-order numerical schemes for wave propagation phenomena," *Intl. J. Num. Methods in Engr.*, vol. 45, pp. 1849–1869, 1999.
- 10 D. Gaitonde, J. S. Shang and J. L. Young, "Practical aspects of high-order accurate finite-volume schemes for electromagnetics," *35th AIAA Aerospace Science Meeting and Exhibit*, AIAA 97-0363, Reno, NV, 1997.

The following research endeavor resulted from a collaboration with Prof. Dennis Sullivan of the University of Idaho, recipient of the U.S. Army Research Office DEPSCoR grant DAAH04-96-1-0406:

- 11 D. Sullivan and J. L. Young, "Far-field time-domain calculation from aperture radiators using FDTD method," *IEEE Trans. Antennas and Propagation* (Submitted).

In addition to the stated research objectives of the contract, the PI also engaged in the authoring of one *invited* publication that is relevant to the general electromagnetic community:

- 12 R. G. Olsen, J. L. Young and D. C. Chang, "Electromagnetic wave propagation on a thin wire above earth," *IEEE Trans. Antennas and Propagation*.

The last entry was an invited submission for the special transactions issue in honor of Prof. James Wait; co-authors Olsen and Chang are fellows of the IEEE.

2.2 Numerical Solvers

Another measurable achievement of this contract is the development of five solvers: 3WB1-RK4 FVTD solver, D4-RK4 FDTD solver, CC4-RK4 solver, C4-LF4 solver and Yee FDTD solver. A synopsis of each of these solvers and some representative results obtained from them is given below. For technical and mathematical details associated with these solvers, consult the publication list under section 2.1 and the appropriate appendices attached to this report.

2.2.1 3WB1-RK4 FVTD Solver

The finite-volume, time-domain (FVTD) solver is based upon a conservation equation of the following form:

$$\frac{\partial \mathbf{U}^a}{\partial t} = \frac{1}{V} \int_S \mathbf{n} \times \mathbf{F} dS, \quad (1)$$

where \mathbf{U}^a is the average value of the solution and $\mathbf{n} \times \mathbf{F}$ is the flux crossing the surface S . (See Appendix A for a comprehensive mathematical treatment of the scheme.) The vectors

\mathbf{U}^a and \mathbf{F} are cast in terms of \mathbf{E} and \mathbf{H} (the electric and magnetic field vectors, respectively) such that the previous equation is a restatement of Maxwell's curl equations in global form.

To accomplish the spatial discretization, a primitive vector is invoked and cast in terms of the average value \mathbf{U}^a . The derivative of this vector is proportional to the surface integral of the right-hand side of Eqn. (1). Thus, the degree of spatial accuracy is directly related to the accuracy of the difference operator that approximates this derivative. The final result is a *reconstructed* value of \mathbf{F} in terms of the average value of \mathbf{U} . One possible operator is the second-order central difference operator (i.e., 2C). Although second-order differences lead to a consistent scheme, they also lead to grid-decoupled solutions. Instead, we adopt the notion of upwind differencing, which was first pioneered by the computational fluid dynamics (CFD) community. To apply upwind differencing and to obtain a stable scheme requires one to examine the eigenvalues and eigenvectors of the flux Jacobian matrices associated with Maxwell's equations. Based upon the sign of these eigenvalues, which indicate the direction of wave propagation along a principle coordinate axis, forward or backward differences are invoked. A third-order spatially accurate scheme is realizable if windward-biased stencils (i.e., 3WB1) are employed. Since the solution is discretized within its domain of influence, the semi-discrete equations are both consistent and grid-coupled.

To advance the equations, the four-stage Runge-Kutta integrator is invoked, which is denoted as RK4. A stability analysis of the combined RK4-3WB1 scheme reveals that a Fourier-stable scheme is achievable for CFL values less than 1.74. This same analysis also provides information on the scheme's dissipation and dispersion errors, which, as with all upwind schemes, is dissipation dominant. The effect of this dissipation is made manifest in the data associated with the patch antenna simulation (to be described in a subsequent paragraph).

Finally, to truncate the computational domain, the incoming tangential flux is set to zero. This type of absorbing boundary condition is first-order accurate since it is based upon a one-dimensional wave equation. However, several numerical tests confirm its adequacy as domain truncation operator.

Based upon the previous description, a code was constructed and thoroughly tested. For representative results obtained from this methodology, first consider a simple problem of a gaussian pulse in a one-dimensional, perfectly conducting cavity. The form of the pulse is $e^{-w^2 t^2}$, where $w = 4.14 \times 10^{10}$ 1/s; this value for w yields a frequency spread in excess of 20 GHz. For the simulation parameters, let $\delta_t = 1.179$ ps and $\delta_x = 0.0005$ m. The pulse is assumed to be traveling at the speed of light. To ascertain both the dissipative and dispersive effects on the pulse, we marched the pulse 11,314 time steps, which is the required time for the pulse to attenuate by ten percent from its initial value; see Figure 1. The slight ripple effect seen in the plot of Figure 1 is to be expected due to dissipation, dispersion and boundary related errors. However, since the pulse has traveled twenty round trips, such effects are certainly anticipated.

To validate the dielectric boundary condition methodology, the problem of a gaussian pulse within a partially filled dielectric cavity is considered; the dielectric has a relative permittivity value of 2.3 and fills the first fifty cells of the 200 cell cavity. The pertinent

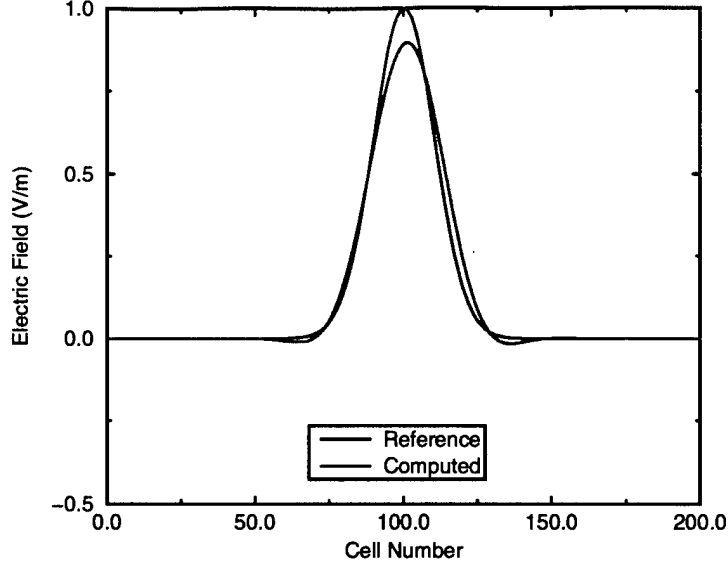


Figure 1: Electric field inside perfectly conducting cavity.

parameters are the same as in the previous example. The initial pulse is centered at cell 100 and is traveling to the left as time advances. Representative results after 230 time steps are provided in Figure 2. As seen directly from the figure, the theoretical transmission coefficient of -0.795 and the theoretical reflection coefficient of -0.205 are predicted.

The one-dimensional problems clearly demonstrate the validity of the FVTD theory. The aforementioned examples demonstrate both the long-term stability of the simulation and the validity of the designed boundary operators for perfectly conducting and dielectric interfaces. For three-dimensional curvilinear domains, the results are not as promising, as discussed next.

The propagation of an electromagnetic wave in a cylindrical waveguide of radius 1 m is the subject of the following discussion; the waveguide is filled with free-space. The domain spans $10 \times 20 \times 100$ cells in ρ , ϕ and z , respectively. The domain is assumed to be periodic in z and the electromagnetic wave is initialized with the TE_{11} time-harmonic mode of frequency $\omega = 2\pi$ r/s. In the radial direction, the signal is sampled at twenty points per wavelength. For this study, let $c = 1$ m/s, $\delta_\rho = 0.1$ m, $\delta_\phi = 2\pi/20$ r, $\delta_z = 5\lambda_z/100 = 0.05229$ m and $\delta_t = 0.01269$ s. Figure 3 shows the magnetic field distribution among various planes within the guide. This figure serves as a qualitative check by showing that the mode has been properly set up within the guide. Next, consider Figures 4 and 5, which show all six components of the electromagnetic signal as a function of radial cell distance at time steps 200 and 2000, respectively. Clearly, the solver is able to predict the basic field phenomenology within the guide. Upon closer examination of the data, however, a small effect of numerical dissipation in the early time and large dissipative effects in the late time are observed. Note: After 2000 times steps, the total energy in the electromagnetic wave has decreased by a factor of three. The highly dissipative nature of the computed solution is consistent with

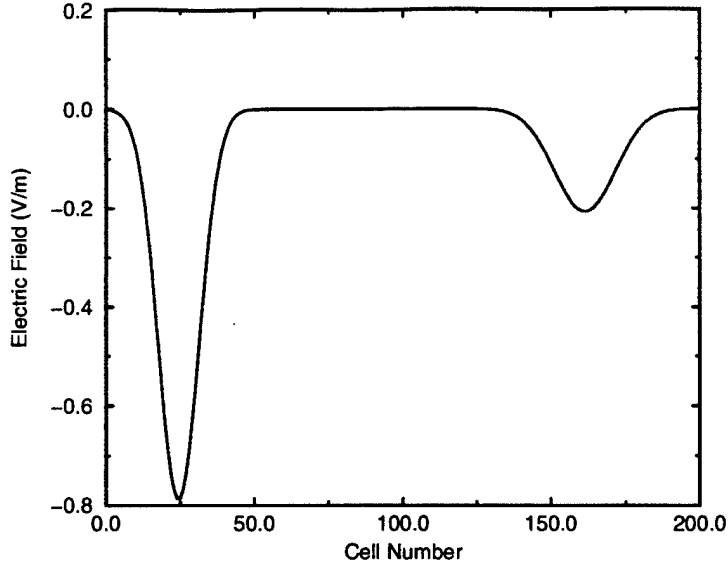


Figure 2: Electric field inside a partially filled dielectric cavity.

the theoretical performance of windward schemes. A second effect is also made manifest in the data: A non-zero longitudinal electric field. The longitudinal component is indeed small relative to its transverse counterparts, which implies that solver has set up a quasi-TE mode rather than a pure TE mode. The generation of this non-physical component is due to the grid and its corresponding metrics. Since each cell is not a parallelepiped, the numerically computed metrics are only second-order accurate (for parallelepiped cells, the metrics are computed exactly.) Hence, the nonlinear terms of the metrics are not captured and the corresponding solution is corrupted by metric-induced errors.

A microstrip transmission line connected to a patch antenna supported by a dielectric of relative permittivity of 2.2 is considered next; see Figure 6. The same parameters suggested in Sheen *et al.* [1] and Luebbers *et al.* [2] are also used here. Specifically, let $\delta_x = .389$ mm, $\delta_y = .400$ mm and $\delta_z = .265$ mm; to insure stability, let $\delta_t = .555$ ps. The patch antenna spans 32 cells by 40 cells; the patch height is 3 cells. The transmission line is chosen to be 20 cells long with the terminal plane placed in the middle of the line. Allowing for some buffering between the absorbing boundary condition and the antenna, we choose the domain size to be $88 \times 111 \times 50$ cells. The voltage excitation is gaussian and of the form $e^{-w^2 t^2}$, where $w = 4.14 \times 10^{10}$ 1/s; this value for w yields a frequency spread in excess of 20 GHz. A 50 Ohm standard is adopted for this simulation. To capture both low- and high-frequency effects, which are manifested in both the late and early time response, the discrete equations are marched 5000 times. Representative field contour plots above and below the patch are shown in Figures 7 and 8, respectively. Numerous plots such as these have been analyzed in detail; the conclusion of that analysis is that the solver is predicting the correct wave behavior and capturing the correct boundary conditions.

Figure 9 shows the calculated input reflection coefficient associated with two solvers: 1)

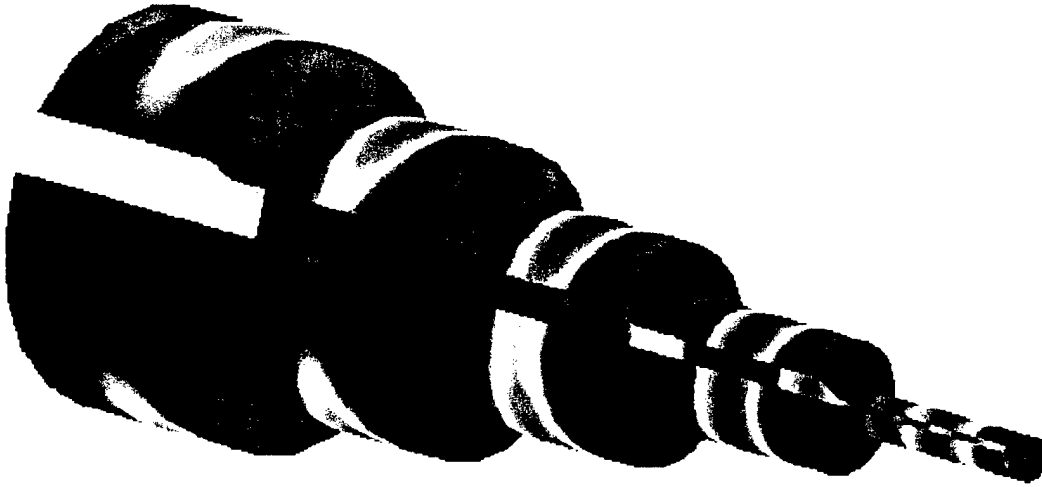


Figure 3: The magnetic field within the cylindrical waveguide.

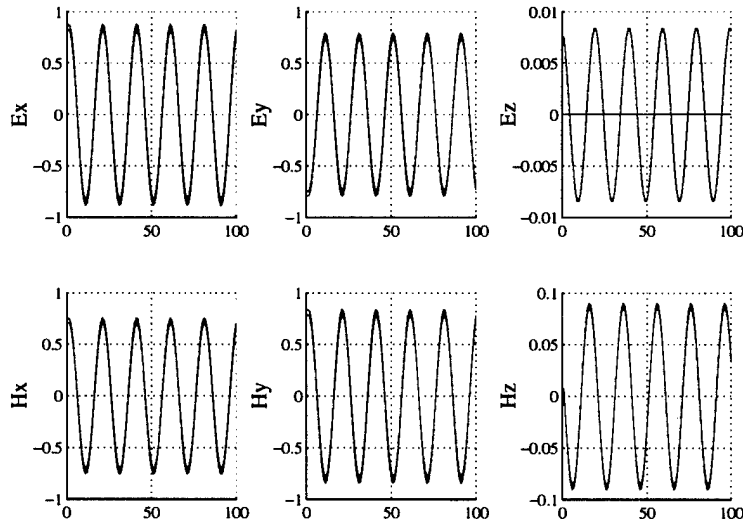


Figure 4: The field components of \mathbf{E} and \mathbf{H} within the cylindrical waveguide at $t = 200\delta_t$. The dotted lines are the analytical solution; the solid lines are the computed solution.

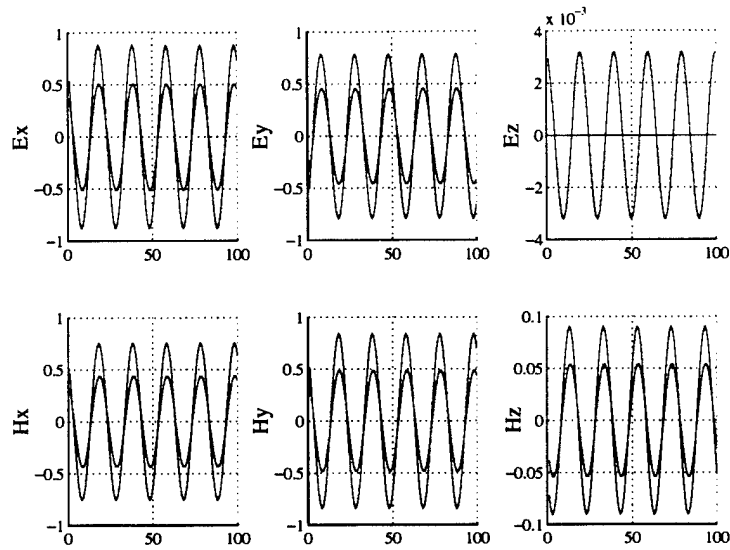


Figure 5: The field components of \mathbf{E} and \mathbf{H} within the cylindrical waveguide at $t = 2,000\delta_t$. The dotted lines are the analytical solution; the solid lines are the computed solution.

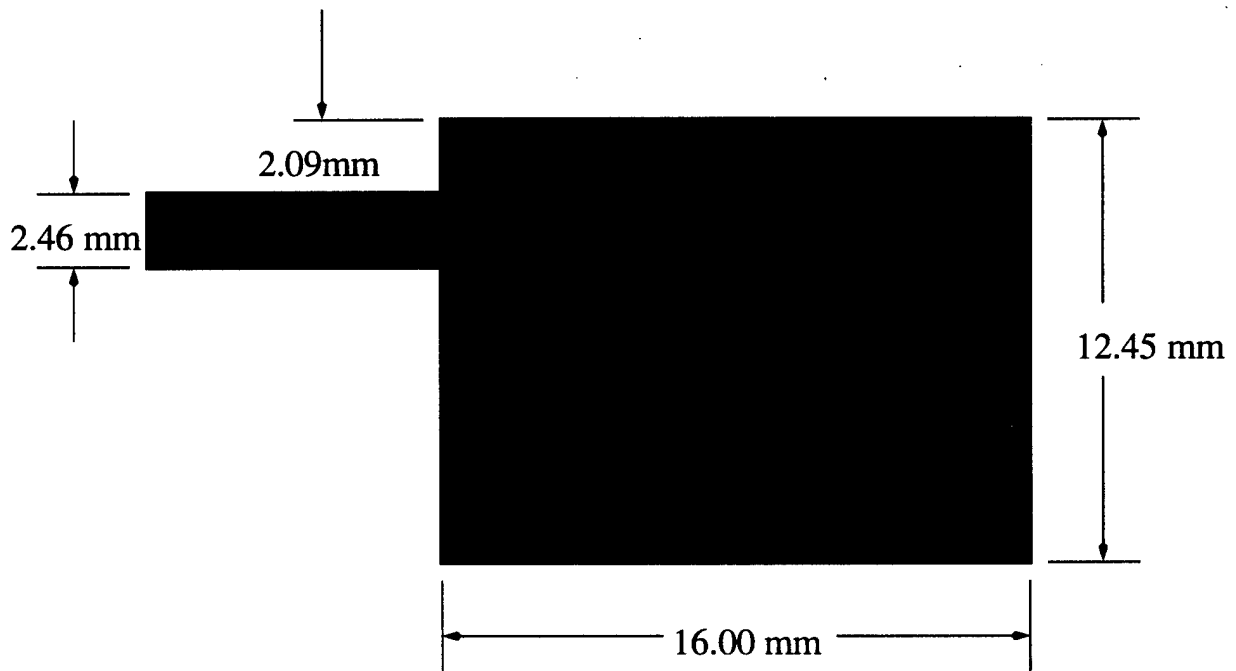


Figure 6: A layout of the patch antenna under consideration.

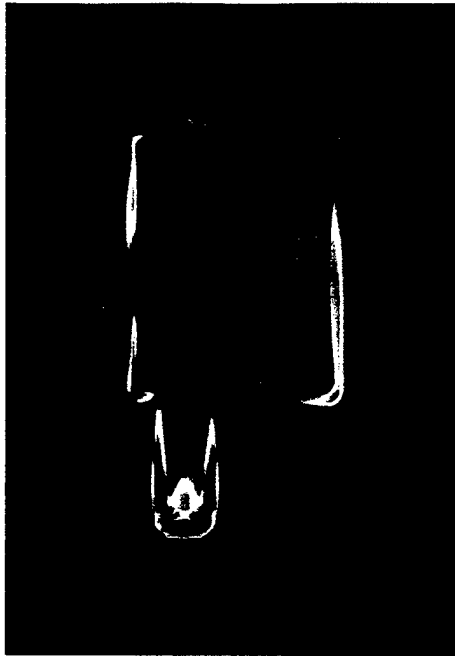


Figure 7: A representative field contour plot above the patch.

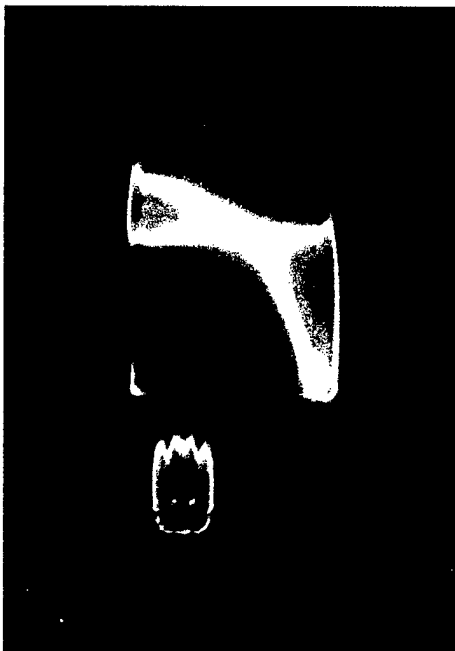


Figure 8: A representative field contour plot below the patch.

Luebbers	Sheen	FDTD	FVTD-1	FVTD-2	Measured
7.51	7.39	7.37	7.13	7.28	7.39
10.04	9.78	9.79	9.31	9.64	9.85
12.13	12.09	11.88	11.72	11.99	N/A
14.66	14.48	14.08	13.72	14.13	14.63
17.91	18.06	17.49	N/A	17.81	18.43
19.78	19.85	19.25	N/A	N/A	20.00

Table 1: Resonant frequencies in GHz for the patch antenna of Figure 2.

the popular Yee FDTD solver and 2) the 3WB1-RK4 FVTD solver. Here FVTD-1 and FDTD have identical numerical parameters. FVTD-2 uses a more refined grid and temporal step size in which $\delta_x = .265$ mm, $\delta_y = .265$ mm, $\delta_z = .0795$ mm and $\delta_t = .2114$ ps; the domain size is $111 \times 154 \times 80$. As Table 1 suggests, both solvers predict the same resonant (or radiation) frequencies of the antenna. These frequencies also compare well with the published resonant frequencies of Sheen *et al.* [1] and Luebbers [2] *et al.*. However, it is also clear from the reflection coefficient data shown in Figure 9 that the data generated by the better of the two finite-volume schemes (i.e., FVTD-2) is anywhere from 2 to 4 dB more dissipative than the data generated by the Yee scheme (and the data measured by Sheen). This observation is expected, due to the highly dissipative nature of the up-wind schemes, and is corroborated by the data associated with the circular waveguide study.

To further emphasize the dissipative nature of the upwind approach, we consider a 50Ω microstrip transmission line. The line is 8 cm long and 0.233 cm wide; the strip is placed on top of a grounded dielectric slab with a relative permittivity of 2.2 and a thickness of .795 mm. For the computational parameters, let $\delta_x = .389$ mm, $\delta_y = .400$ mm, $\delta_z = .265$ mm and $\delta_t = .555$ ps; the computational domain spans $46 \times 240 \times 30$ cells. The microstrip is excited in a similar fashion as the microstrip associated with the patch antenna study. To monitor the propagation of the wave on the line as a function of space, three voltage and three current probes were placed at 2, 4 and 6 cm away from the source. The numerical data gathered by these three probes is plotted in Figure 10. In this figure we see the expected numerically generated dissipation. However, the veracity of the data is confirmed by noting that the voltage and current are proportional to the characteristic impedance of the line. Since both voltage and current dissipate at the same rate down the line, the ratio of 50 Ohms is not impacted by numerical dissipation.

More disconcerting than the dissipation errors of the FVTD solver is the solver's poor computational efficiency. To create the data for the patch antenna study, FVTD-2 took approximately 10.0 hours of Cray T90 CPU time and 108 MW of core memory. In contrast, the FDTD Yee solver, took only 0.05 hours of Cray T90 CPU time and 5.9 MW of core memory. Even if some additional effort were applied to try to improve the computational through-put of the FVTD solver by a factor of ten, it is clear that, for microwave planar circuit applications, the upwind MUSCL approach is inferior.

Since the 3WB1-RK4 finite-volume scheme is nodally collocated and temporally syn-

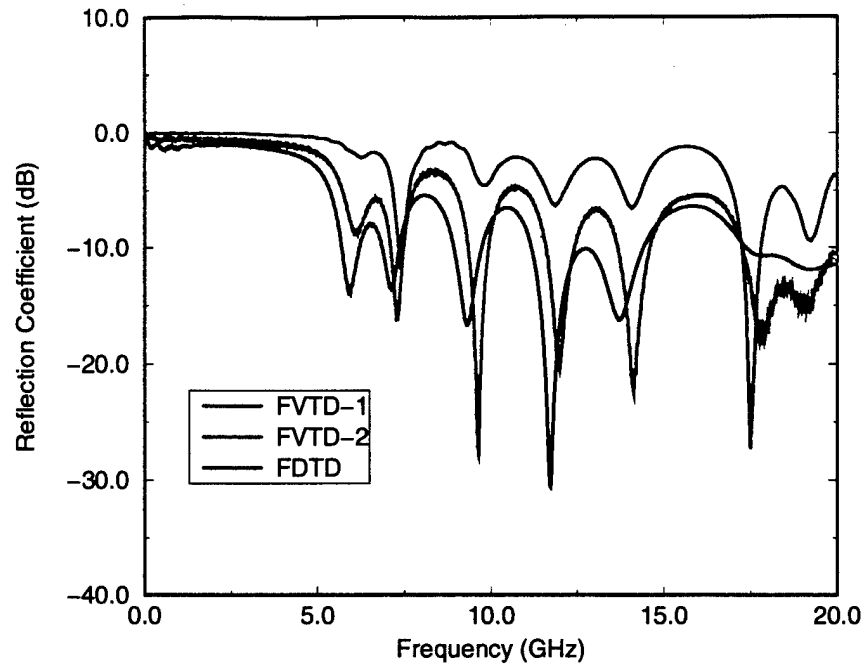


Figure 9: Reflection coefficient data associated with the patch antenna.

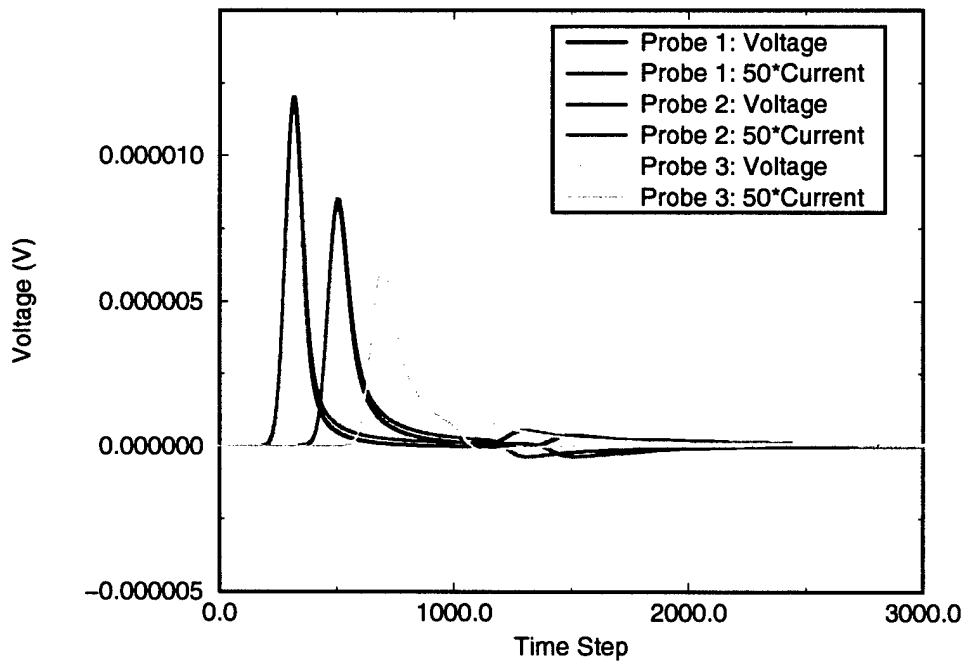


Figure 10: Voltage and current probe data associated with the 50 Ohm microstrip transmission line.

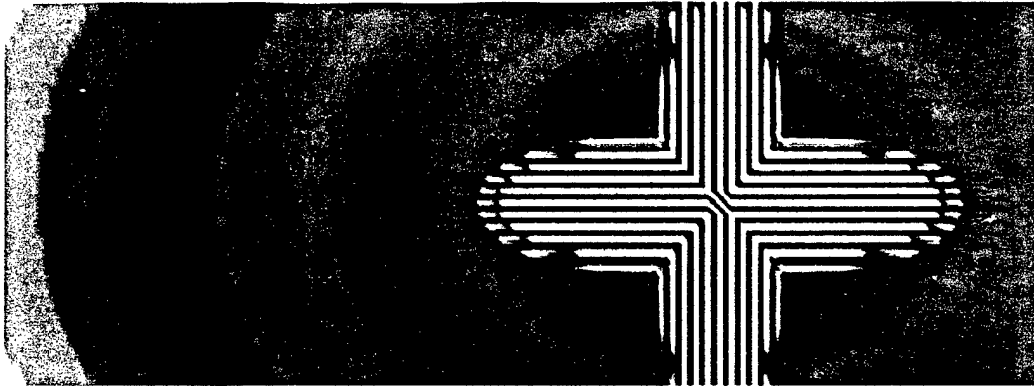


Figure 11: Near-field electromagnetic field data about a line source. The striping of the data suggests strong grid decoupling.

chronized, several algorithmic issues arise. The first issue is the application of boundary conditions at a perfectly conducting interface. In this situation, the scheme requires that both tangential \mathbf{E} and \mathbf{H} be specified on the boundary. However, due to the fact that tangential \mathbf{E} satisfies a Dirichlet condition and tangential \mathbf{H} satisfies a Neumann condition, the boundary conditions associated with this scheme are over-specified. Hence, an incorrect estimate for tangential \mathbf{H} can produce errors in the data or induced instabilities in the simulation. Second, even though upwind schemes are well known to prevent grid decoupling, grid decoupling can be induced via the Runge-Kutta integrator. Since the Runge-Kutta integrator requires that both field components be advanced simultaneously, the excitation of one field component is not made manifest to the other field component at the instant the excitation is applied. This effect is most noticeable when modeling volumetric and sheet sources; the effect is observed near the source, where the data extremely alternates between positive and negative values, as shown in Figure 11.

2.2.2 D4-RK4 FDTD Solver

The fourth-order, finite-difference, time-domain solver, labeled D4-RK4 FDTD, is based upon a procedure that embeds strict, time-stable theorems into the design of high-order boundary operators. To realize a time-stable, fourth-order (in space and time) algorithm, a standard fourth-order Runge-Kutta (RK4) integrator is used to temporally advance the equations; the spatial stencils and boundary operators are designed using summation-by-parts techniques based upon a summation-by-parts energy norm.

To develop the theory, the case of z -directed, one-dimensional propagation is couched in terms of a 2×2 hyperbolic system: $w_t = A w_z$, where $w^T = [E_x cB_y]$ is the solution vector and w_z is the partial derivative of the solution vector with respect to the z -direction. For the specific problem of propagation in a perfectly conducting cavity, the tested spatial discretizations utilize a fourth-order, restricted, full-norm operator (RF4) or a fourth-order diagonal norm operator (D4). For the one-dimensional scalar advection equation, the RF4

operator has the form

$$h Q = \begin{bmatrix} \frac{-11}{6} & 3 & \frac{-3}{2} & \frac{1}{3} & 0 & 0 & 0 & 0 & 0 & 0 & \dots \\ q_{10} & q_{11} & q_{12} & q_{13} & q_{14} & q_{15} & q_{16} & 0 & 0 & 0 & \\ q_{20} & q_{21} & q_{22} & q_{23} & q_{24} & q_{25} & q_{26} & 0 & 0 & 0 & \\ q_{30} & q_{31} & q_{32} & q_{33} & q_{34} & q_{35} & q_{36} & 0 & 0 & 0 & \\ q_{40} & q_{41} & q_{42} & q_{43} & q_{44} & q_{45} & q_{46} & 0 & 0 & 0 & \\ 0 & 0 & 0 & \frac{1}{12} & \frac{-2}{3} & 0 & \frac{2}{3} & \frac{-1}{12} & 0 & 0 & \\ 0 & 0 & 0 & 0 & \frac{1}{12} & \frac{-2}{3} & 0 & \frac{2}{3} & \frac{-1}{12} & 0 & \\ \vdots & & & & & & & & & & \ddots \end{bmatrix} \quad (2)$$

where the coefficients q_{ij} are given in the literature by Strand [4]. The coefficients in Eqn. (2) encompass the transition zone between a third-order windward stencil (i.e., 3W) on the boundary and a fourth-order central operator (i.e., 4C) in the interior. Furthermore, these coefficients are designed so that the spatial discretization satisfies a summation-by-parts energy norm. To introduce the physical boundary conditions and to yield time-stable simulations, both test cases (i.e., RF4 or D4) utilize the orthogonal projection method of Olsson [5].

For two-dimensional TE_z mode propagation in the xy -plane, the Maxwell curl equations are couched in terms of a 3×3 hyperbolic system: $u_t = P_x u_x + P_y u_y$, where $u^T = [E_x \ E_y \ cB_z]$. The previous system is applicable near and on planar boundaries but not on corners, where an ambiguity exists for the outwardly pointing normal. To remove the ambiguity, the system of equations is modified and reformulated into a new scattered-field initial value problem of the form $u_t = P P_x u_x + P P_y u_y + (I - P) \tilde{g}_t$, where \tilde{g} incorporates the boundary condition. Specifically,

$$\begin{bmatrix} \frac{\partial E_x}{\partial t} \\ \frac{\partial E_y}{\partial t} \\ c \frac{\partial B_z}{\partial t} \end{bmatrix} = \begin{bmatrix} -\frac{c^2}{2} \frac{\partial B_z}{\partial x} \\ -\frac{c^2}{2} \frac{\partial B_z}{\partial x} \\ -c \frac{\partial E_y}{\partial x} \end{bmatrix} + \begin{bmatrix} \frac{c^2}{2} \frac{\partial B_z}{\partial y} \\ \frac{c^2}{2} \frac{\partial B_z}{\partial y} \\ c \frac{\partial E_x}{\partial y} \end{bmatrix} + \begin{bmatrix} -\frac{1}{2} \frac{\partial}{\partial t} (E_x^{\text{inc}} - E_y^{\text{inc}}) \\ -\frac{1}{2} \frac{\partial}{\partial t} (E_y^{\text{inc}} - E_x^{\text{inc}}) \\ 0 \end{bmatrix}. \quad (3)$$

The previous equation is valid at the corner of a PEC scatterer with a normal defined as $n = (\pm 1/\sqrt{2}, \pm 1/\sqrt{2})$.

For two-dimensional simulations, the D4 stencil is employed to obtain a semi-discrete approximation of the 3×3 hyperbolic system representing electromagnetic fields TE to z . To properly handle the domain truncation, the perfectly matched layer of Zhao and Cangellaris [6] is used. All simulations for TE_z mode propagation show time-stable results. To test the efficacy of the D4-RK4 scheme, a sample scattering geometry is chosen and results from the D4-RK4 scheme are compared to those obtained from our Yee FDTD solver. Long-time integrations are performed for both schemes to produce surface current data, as shown in Figure 12, for a TE_z pulse obliquely incident on a $2.5\lambda \times 10\lambda$ cylinder. The convergence of the two separate techniques to the same answer provides verification for results obtained

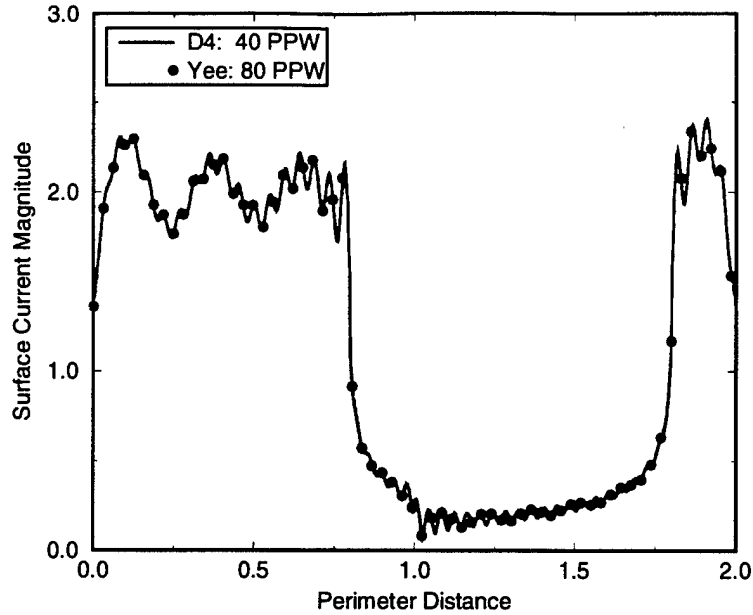


Figure 12: Yee and D4 calculated surface currents for obliquely incident TE_z wave on a $2.5\lambda \times 10\lambda$ cylinder.

from the fully discrete D4-RK4 scheme. A representative contour plot of the electric field is shown in Figure 13; the scatterer in this case is a 10λ square cylinder.

Efforts to expand this theory to three-dimensional geometries are underway. Currently, the three-dimensional version of this code does not yield data that is time stable. We surmise that the boundary operators for a corner of a three-dimensional scatterer are ill-posed and hence, need to be reexamined. An alternative to developing new boundary operators is to develop spatial filters that dampen out high-frequency instabilities. (This technique has been successfully applied by Drs. Shang and Gaitonde of the Air Force Wright Laboratory.) A second option is to invoke high-order differences associated with the Yee grid and the newly developed, fourth-order, leap-frog integrator. Preliminary test cases for this method have been implemented in code; the results of this effort are encouraging. The development of a stable, high-order, three-dimensional finite difference code will continue into the year 2000.

2.2.3 CC4-RK4 Solver

The CC4-RK4 solver utilizes a collocated grid, fourth-order central compact differencing and four stage Runge-Kutta integration. Details associated with this algorithm and code, along with representative data, are available in the following reprint:

J. F. Nystrom and J. L. Young, " k -space transfer function design of discrete operators: Application to Maxwell's time-domain equations," *Journal of Electromagnetic Waves & Applications*, vol. 13, pp. 781-806, 1999.

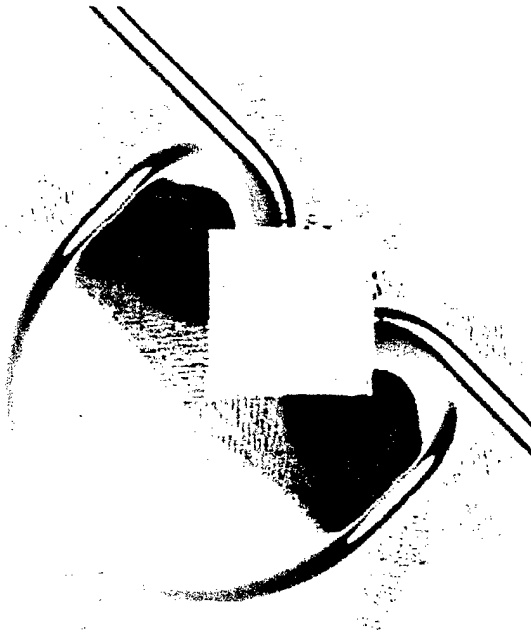


Figure 13: A representative contour plot of the electric field associated with a 10λ square cylinder.

2.2.4 C4-LF4 Solver

The C4-LF4 solver utilizes the Yee grid in conjunction with the newly developed, high-order, leap-frog integrator; consult Appendix B for technical and mathematical details. In principle any even-order accurate spatial stencil of either the implicit or explicit kind may be invoked. However, for purposes of boundary condition implementation, we invoke fourth-order explicit central differences. Since little is to be gained by integrating to a higher-order of accuracy than that of the spatial operators, the leap-frog integrator is limited to fourth-order as well.

The validation of the numerical theory is accomplished by considering wave propagation in a rectangular waveguide. Due to the existence of an exact analytical solution, this problem allows us to conduct precise numerical experiments on a three-dimensional domain structure. Furthermore, this structure requires the algorithm to employ hard boundary conditions on the field vectors at the walls of the waveguide. For the spatially second-order discretization, no special treatment is required to enforce the requisite boundary conditions. With respect to the spatially fourth-order discretization, the cross-sectional domain is extended using image fields. For Dirichlet conditions, the image fields are 180 degrees out of phase with the true fields. For Neumann conditions, the image fields and the true fields are identical in value.

In all cases below, the waveguide's cross-sectional dimensions are $a = b = 1$ m and the excitation angular frequency is 2π r/s; the speed of light is normalized to 1 m/s. For these parameters, the TM_{11} mode is free to propagate and hence, it is the mode under

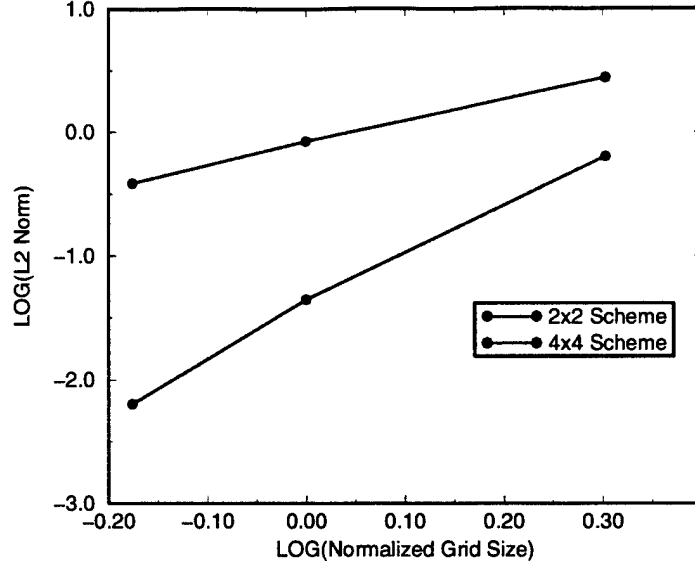


Figure 14: A grid density study of the 2x2 and the 4x4 schemes.

consideration. To avoid any spurious artifacts from the source or from the termination, the waveguide's length is chosen to be exactly $5\lambda_z$, where for the TM_{11} mode, $\lambda_z = \sqrt{2}$ m. In so doing, we create a waveguide that is periodic in the z -direction and hence, we enforce a periodic boundary condition on the source/terminating planes. The field is initialized with the exact solution throughout the entire waveguide.

The first experiment verifies that the codes are performing according to theory. To this end, a grid density study on the 2x2 scheme (i.e., the popular FDTD scheme) and the 4x4 scheme is conducted. The signal in the waveguide is sampled at 5, 10 and 15 points per free-space wavelength in all three directions and the time step is set to one half the value of the cell size. In each experiment, the total number of time steps is adjusted such that the total simulation time is the same, which is arbitrarily chosen to be 25 seconds. The standard \mathcal{L}_2 error norm, averaged over λ_z , is calculated at the end of each simulation and the logarithm thereof is plotted as a function of the logarithm of the cell size. The resulting data is shown in Figure 14. The slope of these curves is the numerical accuracy order of the scheme. For the 2x2 scheme, the end-point to end-point slope is 1.8; for the 4x4 scheme the end-point to end-point slope is 4.2. These values are close enough to the values of two and four, respectively, to conclude that the codes are a true realization of the 2x2 and 4x4 algorithms. Since the 2x4 and 4x2 codes are subsets of the 2x2 and 4x4 codes, no further validation is necessary.

Typical plots of the exact field (i.e. H_z) and the computed fields using the 2x2 and the 4x4 algorithms are shown Figure 15. For these plots, $\delta_x = \delta_y = dz = 0.1$ m and $\delta_t = 0.05$ s. For a frequency of 2π radians, the field is sampled at 10 points per free-space wavelength. The total simulation time is $500\delta_t$. In Figure 15, the anticipated result of significant phase degradation for the 2x2 scheme is obvious; the phase error is 19.2 degrees. As for the 4x4

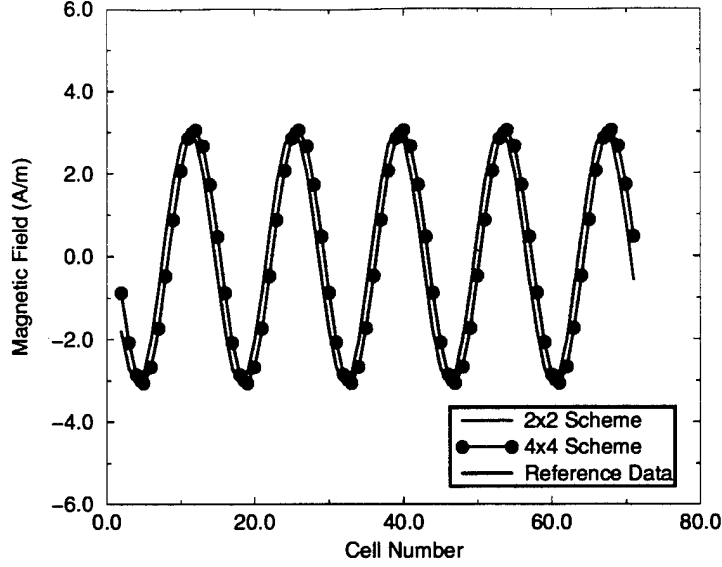


Figure 15: Plots of H_z at $t = 500\delta_t$: $\delta_x = .1\text{m}$ and $\delta_t = .5\delta_x$.

scheme, the phase error is visually imperceptible; its value is only 1.0 degrees. Both schemes show no attenuation of the signal, thereby substantiating the claim that the 2x2 and the 4x4 schemes are dissipationless.

To appreciate the effects of phase error accumulation as a function of time, Figure 16 is provided. From this figure, the slope associated with the 2x2 scheme is 19.2 times that of the 4x4 scheme. This dramatic improvement in phase error accumulation further substantiates the claim that the 4x4 scheme may be used to propagate the signal significantly farther than the 2x2 scheme. For the present scenario, the group energy in the signal has propagated 17.7 free-space wavelengths. The 4x4 scheme can thus propagate the signal 339.8 free-space wavelengths for a duration of $9,600\delta_t$; at the end of the simulation its phase error would also be 19.2 degrees.

Another interesting feature of Figure 16 is the poor phase performance of the 4x2 and 2x4 schemes. Both of the schemes have poorer phase performance relative to the 2x2 scheme. This result for the 4x2 scheme is in agreement with the numerical theory. As for the 2x4 scheme, its poor phase error performance, relative to the phase error of the 2x2 scheme may in part be related to boundary condition induced errors.

2.2.5 Yee FDTD Solver

To establish bench-marking data for all of the aforementioned solvers, the finite-difference, time-domain scheme of Yee and the perfectly match layer concept for open domains was also implemented into numerical code. The procedures for doing so are well-documented in the literature and hence, no detailed description is needed here. This solver was devised and tested on several microstrip planar geometries, including the patch antenna, as confirmed

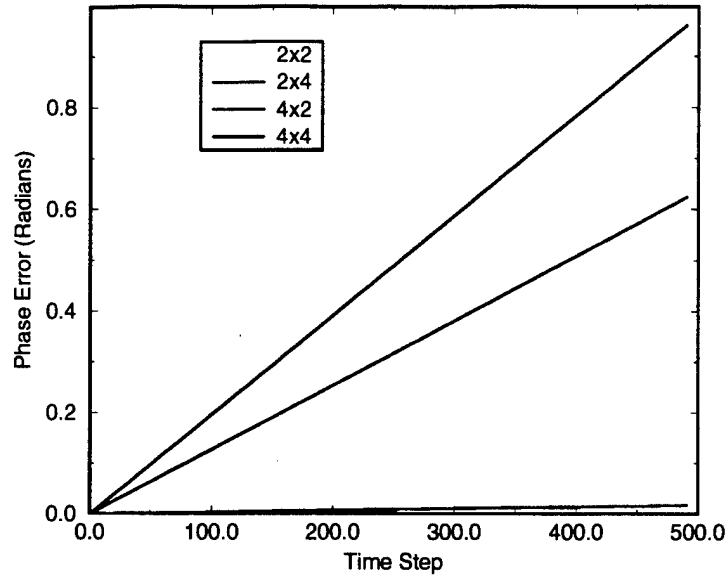


Figure 16: Time-Domain phase error.

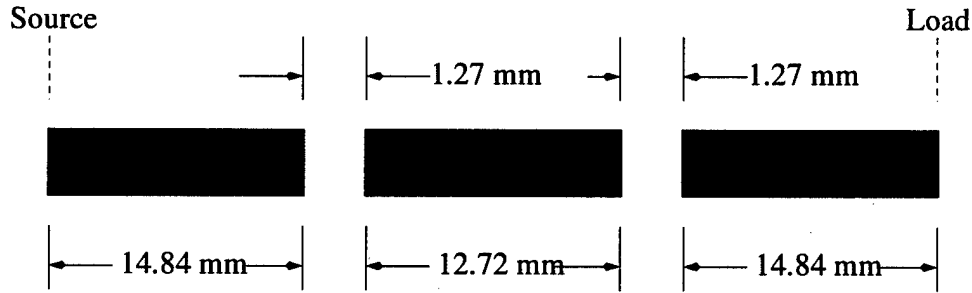


Figure 17: A layout of the band-pass filter under consideration. The substrate thickness is 1.272 mm and its relative permittivity is 9.8.

in section 2.2.1. For further confirmation, consider the band-pass filter configuration of Figure 17. This geometry was programmed into the solver as a sequence of metallic patches, which implies that any geometry made up from an indefinite number of metallic patches (attached or otherwise) could be similarly programmed into code. The source consists of an ideal voltage source in series with a 50 Ohm resistor; both are modeled using quasi-static arguments. The transmission line is terminated with a 50 Ohm load. Letting $\delta_x = 0.212\text{mm}$, $\delta_y = 0.212\text{mm}$, $\delta_z = 0.212\text{mm}$ and $\delta_t = .353\text{ps}$, and running the code for 20,000 time steps, we recorded the total voltage at the input and output ports as a function of time. These values were then transformed into the frequency domain, from which the S_{11} parameters were calculated. The results of this calculation are shown in Figure 18 along with the calculated results of Shibata *et al.* [3]. As expected, the agreement between data sets is quite good. The confirmation between independently generated data sets confirms the bench-marking capability of this solver.

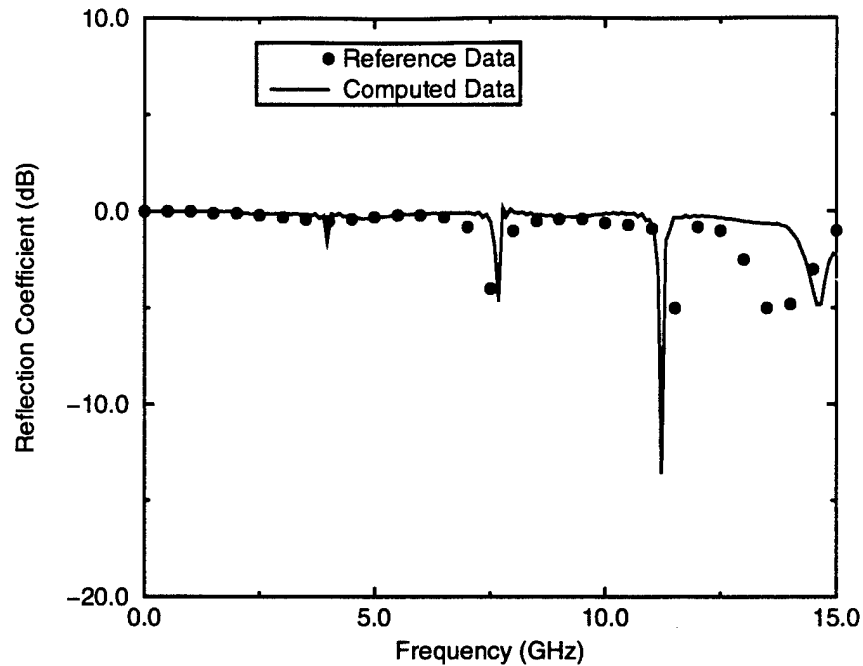


Figure 18: S_{11} data associated with the band-pass filter.

3 Challenges

During the course of the contract, several challenges arose. The most significant ones are outlined below.

3.1 Non-Technical Challenges

There was one non-technical challenge that arose at the beginning of the contract: Graduate student recruitment. Due to tight national labor markets and low enrollments in the university's graduate program, it was difficult to identify, recruit and hire quality graduate students. In the end, the PI was able to hire two outstanding students. However, one was hired in January 1997 and the other in January 1998; thus, the initial progress on this contract was greatly hindered.

3.2 3WB1-RK4 FVTD Solver: Technical Challenges

In the development of the 3WB1-RK4 FVTD solver, several technical challenges were presented to us over the course of the contract. These are briefly articulated below.

Formulation At the beginning of the contract, we adopted the standard, fluid dynamics, conservative form formulation for Maxwell's equations. Although mathematically correct, this form masks many of the physical attributes of the electromagnetic field. Also,

from a software coding point of view, this form requires many redundant and unnecessary computations. Recognizing this, we abandoned this approach and reformulated the finite-volume procedure to manifest the key physical features of the electromagnetic field; see Appendix A for technical details. The final result was a more efficient and robust code than the one that was developed by the PI several years earlier.

Boundary Conditions The nodally collocated scheme places all components of the electric and magnetic field vectors at one location. Hence, there exists ambiguity regarding how to best satisfy the requisite boundary conditions. However, once we adopted our new formulation, this ambiguity was easily resolved.

Grid Decoupling With the hopes of developing a highly efficient scheme, we initially adopted a second-order central difference reconstruction. However, we eventually discovered that such an approach led to grid decoupling, which is most observable when the field is excited by a line source. To prevent decoupling, we adopted a split-flux formulation, which resolved the problem. Unfortunately, grid decoupling can also occur irrespective of the reconstruction; it can also be introduced by the Runge-Kutta integrator. This latter challenge has not been fully resolved at the time of this writing.

Dissipation Extensive numerical tests on one- and two-dimensional geometries were conducted to verify the methodology and the code implementation. These tests predicted the expected result and demonstrated the anticipated numerical errors. However, when the code was applied to the microstrip patch problem and other three-dimensional geometries, significant dissipation was introduced into the solution. All tests conducted so far indicate that this is exclusively an algorithm related error associated with upwind schemes rather than a software coding error.

3.3 D4-RK4 Solver: Technical Challenges

In the development of the D4-RK4 FDTD solver, several technical challenges presented themselves over the course of the contract. These are briefly articulated below.

Domain Truncation Given the desirability of producing highly accurate schemes, the truncation of the open domain became an important issue to address. The decision was made to adopt a perfectly matched layer (PML) approach. Significant effort was applied to deducing a methodology to implement the PML methodology into the RK4 integrator. The final outcome was a precise domain truncation scheme.

Stability It is well known that high-order, three-dimensional, time-stable schemes are difficult to design and implement. To address this fact, two choices were presented to us: 1) to implement a spatial filter to dampen out the high-frequency instabilities, or 2) to use a summation-by-parts formulation and design *a priori stable boundary operators*. Due to the costly computational burden of the former, we chose the latter. Some progress has been made in the design of time-stable solvers. Specifically, this

research is the first to devise a theory and implement that theory for two-dimensional solvers. Of course, more work is needed to devise a methodology for problems that span three dimensions.

Grid Decoupling As with the finite-volume solver, the issue of grid decoupling is of concern in this work as well.

3.4 CC4-RK4 Solver: Technical Challenges

The technical challenges associated with the CC4-RK4 solver are essentially the same as those for the D4-RK4 solver; the reader is referred to section 3.3 for that discussion.

3.5 C4-LF4 Solver: Technical Challenges

The C4-LF4 solver has the most promise of maturing into a solver for mainstream use. Since the scheme is entirely central and staggered in time and space, grid decoupling issues are not encountered. Even though the dominant error mechanism is dispersion, rather than dissipation, numerical case studies indicate that this error mechanism can be mitigated with judicious settings of the numerical parameters. This leaves only boundary condition implementation as the major technical issue to be resolved. This issue is briefly discussed below:

Boundary Conditions One solution that has been considered and tested is the use of compact differences [7]. Here, we can set the boundary conditions for the magnetic field exactly. However, for the electric field, the use of image terms or one-side differences need to be invoked near the boundary. It is not clear at this time if such a solution will yield a stable scheme for all problems of interest. A second approach is to use low-order differences in the direction where the field is slowly varying in space. For example, for the simulation of the electromagnetic field associated with planar circuits, it is well known that the electric and magnetic field slowly varies in the transverse plane relative to the propagation direction. Hence, for this application, a second-order central difference can be applied in the transverse plane and high-order central differences can be applied in the direction of propagation. The resulting scheme would indeed be low-order, but highly accurate.

3.6 Yee FDTD Solver: Technical Challenges

The Yee FDTD solver is based on a very mature foundation of research knowledge. Hence, no real technical challenges arose during the development of the numerical code. Further work is necessary to improve the code's robustness and efficiency.

Model	CPU	RAM	Hard Drive
HP C180	180 MHz	384 MB	4 GB
HP C180	180 MHz	128 MB	4 GB
HP C110	110 MHz	128 MB	4 GB

Table 2: Hewlett-Packard workstations.

Product	Description
Mathematica	Symbolic manipulator package
Field View	Data post-processing colorization plotting package

Table 3: Software tools.

4 Graduate Students

A large portion of the contractual funding was dedicated to the employment of two graduate students: Mr. Ronald Nelson and Mr. James Nystrom. Mr. Nelson was hired in January 1998 and is anticipated to complete his Masters of Science in Electrical Engineering in December 1999. Mr. Nelson's primary task was to develop and test the finite-volume, time-domain solver. Mr. Nystrom was hired in January 1997 and is anticipated to complete his PhD in Electrical Engineering in May 2000. Mr. Nystrom's primary task was to develop and test the high-order finite-difference solver. Mr. Nystrom also played an key role in the development of the k -space design method of discrete operators.

5 Interactions with AFRL Personnel

The obligations set forth in the PI's proposal were performed separate from, but in consultation with, the scientists and engineers of the Air Force Research Laboratory (AFRL), Air Vehicles Directorate. The principle points of contact were Dr. Joseph Shang (Senior Scientist) and Dr. Datta Gaitonde (Research Engineer). Over the past three years, three publications have borne the names of these individuals and the (PI); one manuscript is currently being considered for publication.

6 Facilities

In addition to salaries, contractual funding was also used to acquire equipment and software; see Table 2 for a list of the major equipment purchases and Table 3 for software purchases. Due to these acquisitions, the Laboratory of Applied Computational Electromagnetics is now able to conduct internationally competitive research.

7 Web Page

Computer animations showing the evolution of the electromagnetic field associated with the microstrip patch antenna, microstrip transmission line, the rectangular cylindrical scatter, as well as other geometries, can be found at the following world wide web address:

http://www.mrc.uidaho.edu/mrc/people/nystrom/antennas_1.html.

These color animations were created using the post-processing software tool, Field View, which was procured with contract funds. Not only do such animations provide valuable insight into the phenomenology of the electromagnetic field, they are also valuable in detecting code induced errors in the data sets.

8 Future Work

As mentioned earlier, the development and test of the finite-volume and the finite-difference solvers will be continued by the two graduate students Nelson and Nystrom. It is estimated that this development and testing process will continue into December 1999 for Mr. Nelson and into May 2000 for Mr. Nystrom. No funding will be solicited from the DEPSCoR program office to fund these tasks.

In addition to these two endeavors, efforts are also underway to improve the efficiency, usability and accuracy of our Yee solver. Based upon current research, we believe that the solution accuracy of the solver can be improved by incorporating the PML of Zhao *et al.*

With this DEPSCoR grant, the PI has established the necessary infrastructure to operate a nationally competitive research program. To maintain this program and to further advance the state of knowledge in highly-accurate algorithm development, the PI has submitted a follow-up proposal to the DEPSCoR program office. Due to the many technical deficiencies of the nodally collocated schemes (i.e., dissipation errors, grid decoupling, boundary condition implementation, code inefficiencies, etc.), this new proposal emphasizes the development of highly-accurate, nodally uncollocated schemes and leap-frog integration. Both of these concepts have been examined in detail over the past several years but have not been applied to problems of practical interest. For the microwave circuits and antenna engineer, such problems would include radiation from an array of planar patch antennas or the propagation of an electromagnetic signal through a microstrip circuit. For problems of this nature that are electrically large, both highly accurate and highly efficient numerical solvers are needed. We believe this new thrust has the promise of achieving both.

9 Acknowledgements

The PI and his graduate students acknowledge the strong support that was provided them by the managers, scientists and engineers of the Air Force Office of Scientific Research and the Air Force Research Laboratory. Particularly, gratitude is offered to Dr. Arje Nachman of the

Air Force Office of Scientific Research for his significant efforts to procure financial support for this project. Gratitude is also offered to Dr. Joseph Shang and Dr. Datta Gaitonde for their many technical contributions to this work. Finally, large-scale simulations were conducted on the supercomputers at the DoD's High-Performance Computing Centers.

A Appendix: Finite-Volume Procedure

It is well known that the mathematical description of the electromagnetic field is given as a solution to the two curl and two divergence equations of Maxwell [8]. In the ensuing subsections, a short description of these equations is provided and methods for their discretization are examined in detail in the context of the finite-volume procedure.

Letting \mathbf{E} and \mathbf{H} denote the vector symbols of the electric and magnetic fields, respectively, Maxwell postulated that

$$\mu \frac{\partial \mathbf{H}}{\partial t} + \nabla \times \mathbf{E} = 0, \quad (4)$$

$$\epsilon \frac{\partial \mathbf{E}}{\partial t} - \nabla \times \mathbf{H} = 0, \quad (5)$$

$$\nabla \cdot \mathbf{E} = 0, \quad (6)$$

and

$$\nabla \cdot \mathbf{H} = 0. \quad (7)$$

The previous description assumes that the space under consideration is devoid of sources. In addition, the assumptions that the permittivity ϵ and the permeability μ are scalars and of constant value are made. For purposes of numerical computation, the two curl equations are discretized and advanced in time; the two divergence equations are additional constraints imposed upon the fields.

An alternate form of Maxwell's equations that has significance to certain discretization operators is obtained by adding and subtracting like terms within the two curl equations:

$$\mu \frac{\partial \mathbf{H}}{\partial t} + \nabla \times \mathbf{F}_e^+ + \nabla \times \mathbf{F}_e^- = 0 \quad (8)$$

$$\epsilon \frac{\partial \mathbf{E}}{\partial t} - \nabla \times \mathbf{F}_m^+ - \nabla \times \mathbf{F}_m^- = 0, \quad (9)$$

where

$$\mathbf{F}_e^+ = (\mathbf{E} - \eta \mathbf{n} \times \mathbf{H})/2, \quad (10)$$

$$\mathbf{F}_e^- = (\mathbf{E} + \eta \mathbf{n} \times \mathbf{H})/2, \quad (11)$$

$$\mathbf{F}_m^+ = \frac{1}{2} \left(\mathbf{H} + \frac{\mathbf{n} \times \mathbf{E}}{\eta} \right), \quad (12)$$

and

$$\mathbf{F}_m^- = \frac{1}{2} \left(\mathbf{H} - \frac{\mathbf{n} \times \mathbf{E}}{\eta} \right). \quad (13)$$

In Eqns. (10)–(13), \mathbf{n} is an arbitrary unit vector yet to be specified. Obviously, $\mathbf{F}_e^+ + \mathbf{F}_e^- = \mathbf{E}$ and $\mathbf{F}_m^+ + \mathbf{F}_m^- = \mathbf{H}$, as required. More importantly, for a plane wave traveling in the \mathbf{n} direction, \mathbf{F}_e^- and \mathbf{F}_m^- are identically zero, whereas \mathbf{F}_e^+ and \mathbf{F}_m^+ are not. Likewise, for a plane wave traveling in the negative \mathbf{n} direction, \mathbf{F}_e^+ and \mathbf{F}_m^+ are identically zero, whereas \mathbf{F}_e^- and

\mathbf{F}_m^- are not. Thus, it can be argued that the role of \mathbf{F}_e^+ , \mathbf{F}_m^+ , \mathbf{F}_e^- and \mathbf{F}_m^- is to discriminate between a plane wave traveling in the positive or negative \mathbf{n} directions.

The global form of the governing equations can be obtained by integrating the point-form equations over some volume V . The volume is enclosed by the surface S , which is defined by the outward pointing normal \mathbf{n} . Integrating over V and invoking the vector curl theorem, we obtain

$$\epsilon \frac{\partial \mathbf{E}^a}{\partial t} = \frac{1}{V} \int_S \mathbf{n} \times \mathbf{H} dS \quad (14)$$

and

$$\mu \frac{\partial \mathbf{H}^a}{\partial t} = \frac{1}{V} \int_S \mathbf{E} \times \mathbf{n} dS. \quad (15)$$

Here \mathbf{E}^a and \mathbf{H}^a are the average values of \mathbf{E} and \mathbf{H} , respectively, within the volume V . That is,

$$\mathbf{E}^a = \frac{1}{V} \int_V \mathbf{E} dV \quad (16)$$

and

$$\mathbf{H}^a = \frac{1}{V} \int_V \mathbf{H} dV. \quad (17)$$

A chief attribute of both Eqns. (14) and (15) is the exclusive manifestation of tangential field components on the volume surface. This attribute is compatible with the boundary conditions for \mathbf{E} and \mathbf{H} [8].

The integration of Eqns. (8) and (9) throughout the volume V is accomplished in the exact same manner as in the previous section. The result is

$$\epsilon \frac{\partial \mathbf{E}^a}{\partial t} = \frac{1}{V} \int_S \mathbf{n} \times \mathbf{F}_m^+ dS + \frac{1}{V} \int_S \mathbf{n} \times \mathbf{F}_m^- dS \quad (18)$$

and

$$\mu \frac{\partial \mathbf{H}^a}{\partial t} = \frac{1}{V} \int_S \mathbf{F}_e^+ \times \mathbf{n} dS + \frac{1}{V} \int_S \mathbf{F}_e^- \times \mathbf{n} dS. \quad (19)$$

The unit vector \mathbf{n} in Eqns. (10)–(13) is now defined to be the vector normal to the surface S .

Given the similarity of Eqns. (14), (15), (18), and (19), we consider the following canonical integral equation as the basis for the ensuing mathematical development:

$$\frac{\partial \mathbf{U}^a}{\partial t} = \frac{1}{V} \int_S \mathbf{n} \times \mathbf{F} dS \quad (20)$$

where \mathbf{U}^a denotes either $\epsilon \mathbf{E}^a$ or $\mu \mathbf{H}^a$; \mathbf{F} denotes either $-\mathbf{E}$, \mathbf{H} , $-\mathbf{F}_e^+ - \mathbf{F}_e^-$ or $\mathbf{F}_m^+ + \mathbf{F}_m^-$, depending upon the context. Also, in anticipation of the numerical procedure, the volume V is assumed to be comprised of six faces S_1, S_2, \dots, S_6 ; the sum of these faces is the closed surface S . For a six-sided volume, Eqn. (20) reduces to

$$\frac{\partial \mathbf{U}^a}{\partial t} = \frac{1}{V} \sum_{l=1}^6 \mathbf{I}_l \quad (21)$$

where

$$\mathbf{I}_l = \int_{S_l} \mathbf{n}_l \times \mathbf{F} dS; \quad (22)$$

here \mathbf{n}_l is the outward-pointing normal to S_l .

The evaluation of the integrals in Eqn. (21) is facilitated by establishing a curvilinear transformation that maps V into V' , the transformed region of integration. The mapping is accomplished through the following equations: $\xi = \xi(x, y, z)$, $\eta = \eta(x, y, z)$ and $\zeta = \zeta(x, y, z)$. By invoking the Jacobian J , we compute the average value via

$$\mathbf{U}^a = \frac{1}{V} \int_{V'} \mathbf{U}' J d\xi d\eta d\zeta; \quad (23)$$

here $\mathbf{U}'(\xi, \eta, \zeta, t) = \mathbf{U}(x(\xi, \eta, \zeta), y(\xi, \eta, \zeta), z(\xi, \eta, \zeta), t)$.

Next consider the integration over the six faces. The surfaces S_1, S_2, S_3, S_4, S_5 and S_6 are defined by $\xi = \xi_1$ (ξ_1 is a constant), $\xi = \xi_2$, $\eta = \eta_1$, $\eta = \eta_2$, $\zeta = \zeta_1$ and $\zeta = \zeta_2$, respectively. One of these surfaces, say S_2 and its integral \mathbf{I}_2 , is the focus of the following development; the remaining five surface integrals are evaluated in a similar fashion. Considering Eqn. (22) for $l = 2$, we obtain, through a change of variables the equation,

$$\mathbf{I}_2 = \int_{S'_2} \mathbf{n}_2 \times \mathbf{F}'(\xi_2, \eta, \zeta, t) J |\nabla \xi| d\eta d\zeta, \quad (24)$$

where $\mathbf{F}'(\xi, \eta, \zeta, t) = \mathbf{F}(x(\xi, \eta, \zeta), y(\xi, \eta, \zeta), z(\xi, \eta, \zeta), t)$ and S'_2 is the transformed region associated with S_2 . Since $\nabla \xi$ is perpendicular to surfaces of constant ξ , $\mathbf{n}_2 |\nabla \xi| = \nabla \xi$ and

$$\mathbf{I}_2 = \int_{S'_2} \nabla \xi \times \mathbf{F}'(\xi_2, \eta, \zeta, t) J d\eta d\zeta. \quad (25)$$

One approach towards evaluating \mathbf{I}_2 from known cell average values consists of introducing a primitive vector \mathbf{W} , whose derivative is \mathbf{I}_2 [9]. Stated mathematically,

$$\frac{\partial \mathbf{W}_2}{\partial \xi} \equiv \mathbf{I}_2 \quad (26)$$

Primitive vectors for the other surface integrals are defined in a similar manner. It is apparent from the above equation that value of the surface integral hinges upon the mechanism for computing the primitive vector and its derivative.

Values for the primitive vector are deduced by considering a more general definition for its derivative than the one provided by Eqn. (26). Let

$$\frac{\partial \mathbf{W}(\xi)}{\partial \xi} = \int_{S'(\xi)} \nabla \xi \times \mathbf{F}'(\xi, \eta, \zeta) J d\eta d\zeta. \quad (27)$$

From this definition, it follows that $S'(\xi_2) = S'_2$ and

$$\left. \frac{\partial \mathbf{W}(\xi)}{\partial \xi} \right|_{\xi=\xi_2} = \frac{\partial \mathbf{W}_2}{\partial \xi}. \quad (28)$$

Then, by means of Riemann integration of Eqn. (27),

$$\mathbf{W}(\xi) = \mathbf{W}(\xi_1) + \int_{\xi_1}^{\xi} \int_{S'(\tau)} \nabla \xi \times \mathbf{F}'(\tau, \eta, \zeta) J d\eta d\zeta d\tau. \quad (29)$$

The evaluation of this integral at $\xi = \xi_2$ yields

$$\mathbf{W}(\xi_2) = \mathbf{W}(\xi_1) + \int_{\xi_1}^{\xi_2} \int_{S'(\tau)} \nabla \xi \times \mathbf{F}'(\tau, \eta, \zeta) J d\eta d\zeta d\tau. \quad (30)$$

By definition the integration term is proportional to the average value of $\nabla \xi \times \mathbf{F}$ over the volume V and hence,

$$\mathbf{W}(\xi_2) = \mathbf{W}(\xi_1) + V(\nabla \xi \times \mathbf{F})^a. \quad (31)$$

The antecedent equation fundamentally states that the *exact* value of \mathbf{W} at domain walls can be determined from the *average* value of $\nabla \xi \times \mathbf{F}$ within that domain.

The previous equation is exact, provided that the metric information associated with $\nabla \xi$ is known exactly. To compute the metrics, a mathematical description of the ξ is required. Consider the description $\xi = \xi_l + \xi_n$, where ξ_l and ξ_n represent the linear and non-linear terms of ξ , respectively. Since $\nabla \xi_l$ is constant, it follows from Eqn. (31) that

$$\mathbf{W}(\xi_2) = \mathbf{W}(\xi_1) + V \nabla \xi_l \times \mathbf{F}^a + V(\nabla \xi_n \times \mathbf{F})^a. \quad (32)$$

If $\nabla \xi_n$ is regarded as sufficiently small throughout the volume, then

$$\mathbf{W}(\xi_2) \approx \mathbf{W}(\xi_1) + V \nabla \xi_l \times \mathbf{F}^a, \quad (33)$$

which is a second-order approximation. The error of this approximation ε is obtained by the mean value theorem of integral calculus:

$$\varepsilon = \mathbf{F}'(\xi_o, \eta_o, \zeta_o) \int_{V'} \nabla \xi_n d\xi d\eta d\zeta, \quad (34)$$

where ξ_o, η_o, ζ_o is some point in the volume V' . For volumes that are parallelepipeds, $\varepsilon = 0$.

A value for $\nabla \xi_l$ can be obtained from the geometry of the volume. In a separate note, we show that $\nabla \xi \approx \delta_\xi \mathbf{A}_\xi^a / V$, where δ_ξ is the distance between S_1 and S_2 and \mathbf{A}_ξ^a is the average directed surface area in the ξ direction within V . By definition,

$$\mathbf{A}_\xi^a = \frac{1}{\delta_\xi} \int_{\xi_1}^{\xi_2} \mathbf{A}(\xi) d\xi. \quad (35)$$

Therefore, Eqn. (33) reduces to

$$\mathbf{W}(\xi_2) \approx \mathbf{W}(\xi_1) + \delta_\xi \mathbf{A}_\xi^a \times \mathbf{F}^a, \quad (36)$$

Due to the simplicity of the Eqn. (36), the code development for the primitive vector is trivial.

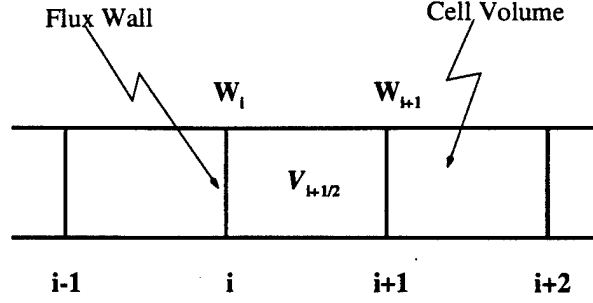


Figure 19: A pictorial representation of the indexing scheme used in the flux reconstruction.

To obtain an approximation for the derivative of the primitive vector, the domain V is sub-divided into many sub-volumes, each denoted as $V_{i-1/2,j-1/2,k-1/2}$; Eqn. (21) is now an equation over each sub-domain. The six surfaces defining each sub-volume are still denoted locally as S_1 through S_6 . Globally, the surfaces S_1 and S_2 are defined by the equations $\xi = \xi_{i-1}$ and $\xi = \xi_i$, respectively. Likewise, $\eta = \eta_{j-1}$, $\eta = \eta_j$, $\zeta = \zeta_{k-1}$ and $\zeta = \zeta_k$ globally define S_3, S_4, S_5 and S_6 , respectively. Using this notation, we cast Eqn. (31) as follows:

$$\mathbf{W}_i = \mathbf{W}_{i-1} + V_{i-1/2}(\nabla\xi \times \mathbf{F})_{i-1/2}^a, \quad 1 \leq i \leq I_{\text{pts}} \quad (37)$$

where $(\nabla\xi \times \mathbf{F})_{i-1/2}^a$ is the average value of $\nabla\xi \times \mathbf{F}$ in the volume $V_{i-1/2}$ defined by the grid lines $i-1$ and i . (The indices j, k are dropped for clarity; see Figure 19 for a one-dimensional depiction.) Since \mathbf{W} is to be differentiated, \mathbf{W}_0 may be set to zero, or to any other value.

To estimate the derivative of \mathbf{W} at the cell surface i (i.e., the value of I_2), we simply employ standard difference stencils. For example, a second-order central approximation is given by

$$\left. \frac{\partial \mathbf{W}}{\partial \xi} \right|_i \approx \left(\frac{\mathbf{W}_{i+1} - \mathbf{W}_{i-1}}{2\delta_\xi} \right). \quad (38)$$

Substituting Eqn. (37) in Eqn. (38), we obtain

$$\left. \frac{\partial \mathbf{W}}{\partial \xi} \right|_i \approx \frac{V_{i+1/2}(\nabla\xi \times \mathbf{F})_{i+1/2}^a + V_{i-1/2}(\nabla\xi \times \mathbf{F})_{i-1/2}^a}{2\delta_\xi} \quad (39)$$

Under the assumption that the metrics are computed to second-order,

$$\left. \frac{\partial \mathbf{W}}{\partial \xi} \right|_i \approx \left(\frac{(\mathbf{A}_\xi^a \times \mathbf{F}^a)_{i+1/2} + (\mathbf{A}_\xi^a \times \mathbf{F}^a)_{i-1/2}}{2} \right), \quad (40)$$

where $(\mathbf{A}_\xi^a \times \mathbf{F}^a)_{i\pm 1/2}$ is the average value of \mathbf{A}_ξ in volume $i \pm 1/2$ crossed into the average value of \mathbf{F} in volume $i \pm 1/2$. Eqn. (40) is valid for cells of unequal size or for stretched grids. For uniform grids, it seems reasonable to replace Eqn. (40) with

$$\left. \frac{\partial \mathbf{W}}{\partial \xi} \right|_i \approx \mathbf{A}_i \times \left(\frac{\mathbf{F}_{i+1/2}^a + \mathbf{F}_{i-1/2}^a}{2} \right). \quad (41)$$

Per Eqn. (26), the right hand side of Eqn. (41) is an estimated value of the surface integral I_2 . The equation states that the value of the surface integral is *reconstructed* from average values of \mathbf{F} .

The previous equation is recognized as being nothing more than a central average reconstruction and is one of many reconstruction formulas. As with the primitive vector, its computation is trivial. Within this equation, there exists two approximations. The first is associated with the discretization of the derivative of the primitive vector. The second is associated with the accuracy of the metric computation. Both of these approximations influence the overall accuracy of the reconstructed value. Instead of using a second-order central derivative, a fourth-order central derivative could be employed. If however, the metric is computed to second-order, the reconstructed value is strictly second-order. For cells that are near parallelepipeds, the non-linear metric terms are negligible and the accuracy of the reconstructed value is strongly influenced by the accuracy of the derivative calculation. Thus, even if the scheme is not strictly high-order, it still may be highly accurate.

One difficulty with the employment of central differences for the calculation of the primitive vector derivative (in conjunction with nodally collocated schemes) is the problem of grid decoupling [10]. Since a central operator has holes in its stencil, the unknown and its derivative at a node are decoupled from each other. For point-source excitation, the result of this effect is an interlacement of zeros in the data [11]. To overcome this problem, we consider a split flux treatment, which discretizes \mathbf{F}^+ and \mathbf{F}^- , rather than \mathbf{F} [12]. Since $\mathbf{F} = \mathbf{F}^+ + \mathbf{F}^-$, it follows from Eqn. (37) that $\mathbf{W} = \mathbf{W}^+ + \mathbf{W}^-$, where

$$\mathbf{W}_i^+ = \mathbf{W}_{i-1}^+ + (\nabla \xi \times \mathbf{F}^+)_{i-1/2}^a, \quad 1 \leq i \leq I_{\text{pts}} \quad (42)$$

and

$$\mathbf{W}_i^- = \mathbf{W}_{i-1}^- + (\nabla \xi \times \mathbf{F}^-)_{i-1/2}^a, \quad 1 \leq i \leq I_{\text{pts}} \quad (43)$$

The differentiation of \mathbf{W}^+ and \mathbf{W}^- is accomplished by establishing difference stencils within the domain of influence of these two vectors. That is, for the positive-going waves (i.e., \mathbf{F}^+), backward stencils are invoked; for the negative-going waves (i.e., \mathbf{F}^-), forward stencils are invoked. For example, a second-order windward approximation yields

$$\frac{\partial \mathbf{W}^+}{\partial \xi} \Big|_i \approx \left(\frac{3\mathbf{W}_i^+ - 4\mathbf{W}_{i-1}^+ + \mathbf{W}_{i-2}^+}{2\delta_\xi} \right) \quad (44)$$

and

$$\frac{\partial \mathbf{W}^-}{\partial \xi} \Big|_i \approx \left(\frac{-3\mathbf{W}_i^- + 4\mathbf{W}_{i+1}^- - \mathbf{W}_{i+2}^-}{2\delta_\xi} \right). \quad (45)$$

For second-order metrics, the final result, as obtained from the previous equations and expressed in terms of \mathbf{F}^a , is

$$\frac{\partial \mathbf{W}^+}{\partial \xi} \Big|_i \approx \mathbf{A}_i \times \left(\frac{3(\mathbf{F}^+)_{i-1/2}^a - (\mathbf{F}^+)_{i-3/2}^a}{2} \right), \quad (46)$$

and

$$\frac{\partial \mathbf{W}^-}{\partial \xi} \Big|_i \approx \mathbf{A}_i \times \left(\frac{3(\mathbf{F}^-)_{i+1/2}^a - (\mathbf{F}^-)_{i+3/2}^a}{2} \right), \quad (47)$$

The sum of these two derivatives is the derivative of the total primitive vector (or, the value of the surface integral under investigation.)

A table of commonly used stencils that may be invoked for the derivative of \mathbf{W} , \mathbf{W}^+ or \mathbf{W}^- may be found in many texts (e.g., [13]). Other stencils that are neither central or strictly forward (or backward) can also be constructed via standard Taylor series analysis. For such stencils, we denote them as windward biased. In the numerical examples section, we choose to adopt the third-order windward biased stencil (3WB1) as the stencil under investigation. That is, let

$$\frac{\partial \mathbf{W}^+}{\partial \xi} \Big|_i \approx \left(\frac{2\mathbf{W}_{i+1}^+ + 3\mathbf{W}_i^+ - 6\mathbf{W}_{i-1}^+ + \mathbf{W}_{i-2}^+}{6\delta_\xi} \right) \quad (48)$$

and

$$\frac{\partial \mathbf{W}^-}{\partial \xi} \Big|_i \approx \left(\frac{-2\mathbf{W}_{i-1}^- - 3\mathbf{W}_i^- + 6\mathbf{W}_{i+1}^- - \mathbf{W}_{i+2}^-}{6\delta_\xi} \right). \quad (49)$$

Based upon stability arguments and four-stage Runge-Kutta integration, central differences may be used for either \mathbf{W} , \mathbf{W}^+ or \mathbf{W}^- . Windward and windward biased stencils are typically used for only \mathbf{W}^+ or \mathbf{W}^- .

This section is closed by noting that all of the difference stencils discussed so far are of the explicit type. An alternative to explicit differencing is implicit differencing, or compact differencing. For example, consider the following central compact operator [14, 15]:

$$\alpha \mathbf{Q}_{i+1} + \mathbf{Q}_i + \alpha \mathbf{Q}_{i-1} = \beta (\mathbf{W}_{i+1} - \mathbf{W}_{i-1}). \quad (50)$$

If $\alpha = 1/4$ and $\beta = 3/4$, then \mathbf{Q}_i is approximately the derivative of \mathbf{W} at i ; the degree of approximation is fourth-order. Unlike the fourth-order explicit central operator, which has a stencil that spans five cells, the fourth-order compact operator spans only three cells. This attribute is often quoted in the context of boundary operator implementation. Although the above equation represents a tri-diagonal matrix equation, the solution of that equation is easily obtained by employing the Thomas algorithm [16]. The number of operations associated with the computation of \mathbf{Q}_i is five.

In addition to the equations that govern propagation, Maxwell's equations in global form require that tangential \mathbf{E} and \mathbf{H} be continuous across a dielectric interface. At a perfect electrical conductor defined by the normal \mathbf{n} there exist two conditions of interest:

$$\mathbf{n} \times \mathbf{E} = 0 \quad \mathbf{n} \times \nabla \times \mathbf{H} = 0. \quad (51)$$

These equations are equivalent to

$$\mathbf{E}_t = 0 \quad \frac{\partial \mathbf{H}_t}{\partial n} = 0, \quad (52)$$

where the subscript t denotes the tangential component. Although other boundary conditions may be derived, uniqueness of solution is assured when the tangential fields are specified on the boundary. Moreover, the boundary conditions are compatible with the integrand of the surface integrals, which highlights an important feature of the nodally collocated finite-volume procedure. The algorithmic implementation of these boundary conditions is considered next.

Suppose that $i = 0$ (locally defined surface S_1) resides on a perfect electric conductor (PEC) and the domain is specified by $i \geq 0$. If the integrand of \mathbf{I}_1 is a function of tangential \mathbf{E} , then $\mathbf{I}_1 \equiv 0$. If the integrand of \mathbf{I}_1 is a function of tangential \mathbf{H} , then from the identity

$$\frac{\partial \mathbf{W}_1}{\partial \xi} = \frac{1}{V} \int_{S_1} \mathbf{n}_1 \times \mathbf{H} dS, \quad (53)$$

it follows that a Neumann condition is implemented by setting

$$\frac{\partial^2 \mathbf{W}_1}{\partial \xi^2} = 0 \quad \text{on } S_1. \quad (54)$$

To second-order, this condition is satisfied by employing an image term $\mathbf{W}_1(-1)$ and by setting that image term to the value of $2\mathbf{W}_1(0) - \mathbf{W}(1)$. With this image term, second-order central (2C) or 3WB1 operators can be invoked on the boundary; second-order windward (2W) or 3WB1 operators can be invoked one cell in from the boundary. Note: For the case when 3WB1 operators are used in the interior and 2C operators are used on the boundary, the global spatial accuracy is still third-order [17].

For the situation when S_1 resides on a dielectric interface, at least two possibilities arise. The fact that the tangential fields are continuous across the interface (but a discontinuous first derivative) allows one to reconstruct at that interface with second-order central averages; the reconstruction is in non-split form. In split form, the process of reconstruction is more complicated. The complication arises from the discontinuity of \mathbf{F} , due to the η term. To handle this discontinuity, the primitive vectors associated with \mathbf{E} and \mathbf{H} are built as before. However, two values of \mathbf{F} (i.e., two values of \mathbf{F}^+ and two values of \mathbf{F}^-) must be deduced, depending upon the cell under consideration. To the left of S_1 , \mathbf{F} is a function of η_a ; this \mathbf{F} is used in the time advancement of $\mathbf{U}_{i-1/2}^a$. To the right of S_1 , \mathbf{F} is a function of η_b ; this \mathbf{F} is used in the time advancement of $\mathbf{U}_{i+1/2}^a$.

The truncation of the domain or the development of an absorbing boundary condition (ABC) can be accomplished by several means. The perfectly matched layer (PML) is one such possibility [6]. The development of such a PML for high-order FVTD schemes is the subject of future work. In this work, characteristic theory is adopted for simplicity. In split flux form, we have already noted that \mathbf{F}^+ and \mathbf{F}^- only act on positive- and negative-going waves, respectively. Thus a suitable ABC can be devised by setting either \mathbf{F}^+ or \mathbf{F}^- to zero, depending upon which vector represents an out-going wave.

Upon completion of the reconstruction phase, the semi-discrete equations take on the form

$$\frac{\partial \mathbf{u}}{\partial t} = \mathbf{A} \mathbf{u}, \quad (55)$$

which constitutes a constant coefficient, linear system of ordinary differential equations. Here \mathbf{u} represents every value of \mathbf{U}^a throughout the computational domain and \mathbf{A} is the connectivity matrix. Since our desire is to obtain high-order accuracy, the classical four-stage scheme is invoked and labeled as RK4. In vector form and in terms of the auxiliary vectors $\mathbf{k}_1 \cdots \mathbf{k}_4$, the standard RK4 scheme is as follows [18]:

$$\begin{aligned} \mathbf{k}_1 &= \delta_t \mathbf{A} \mathbf{u}^n \\ \mathbf{k}_2 &= \delta_t \mathbf{A} (\mathbf{u}^n + \mathbf{k}_1/2) \\ \mathbf{k}_3 &= \delta_t \mathbf{A} (\mathbf{u}^n + \mathbf{k}_2/2) \\ \mathbf{k}_4 &= \delta_t \mathbf{A} (\mathbf{u}^n + \mathbf{k}_3) \\ \mathbf{u}^{n+1} &= \mathbf{u}^n + (\mathbf{k}_1 + 2\mathbf{k}_2 + 2\mathbf{k}_3 + \mathbf{k}_4)/6. \end{aligned} \quad (56)$$

Other techniques for low storage RK integrators are reported in the literature [19, 20]. Upon the incorporation of all four stages into the equation for \mathbf{u}^{n+1} , the final result is

$$\mathbf{u}^{n+1} = \left(1 + \delta_t \mathbf{A} + \frac{\delta_t^2}{2} \mathbf{A}^2 + \frac{\delta_t^3}{6} \mathbf{A}^3 + \frac{\delta_t^4}{24} \mathbf{A}^4 \right) \mathbf{u}^n. \quad (57)$$

Furthermore, by substituting Eqn. (55) into Eqn. (57), we obtain

$$\mathbf{u}^{n+1} = \left(1 + \delta_t \frac{\partial}{\partial t} + \frac{\delta_t^2}{2} \frac{\partial^2}{\partial t^2} + \frac{\delta_t^3}{6} \frac{\partial^3}{\partial t^3} + \frac{\delta_t^4}{24} \frac{\partial^4}{\partial t^4} \right) \mathbf{u}^n, \quad (58)$$

which is the expected truncated Taylor series. These two equations reveal the main sources of error: 1) Spatial discretization errors incorporated in the approximation of $\partial \mathbf{u} / \partial t$ by $\mathbf{A} \mathbf{u}$ and 2) temporal errors as a result of the truncated Taylor series. The manifestations of these errors, usually couched in terms of dissipation and dispersion errors, are best characterized in the frequency domain. Since such an analysis has been provided in many sources, we only note that the predominant error mechanism is dissipation [14].

One final note: Even though upwind schemes are well known to prevent grid decoupling, grid decoupling can be induced via the Runge-Kutta integrator. Since the Runge-Kutta integrator requires that both field components be advanced simultaneously, the excitation of one field component is not made manifest to the other field component at the instant the excitation is applied. This effect is most noticeable when modeling volumetric and sheet sources; the effect is observed near the source, where the data extremely alternates between positive and negative values.

B Appendix: High-Order Leap-Frog Integrator

Consider Maxwell's equations for a lossless isotropic homogeneous medium that is described by the permittivity and permeability parameters ϵ and μ , respectively; the medium is also devoid of sources:

$$\epsilon \frac{\partial \mathbf{E}}{\partial t} = \nabla \times \mathbf{H} \quad (59)$$

and

$$\mu \frac{\partial \mathbf{H}}{\partial t} = -\nabla \times \mathbf{E}. \quad (60)$$

Here \mathbf{E} and \mathbf{H} are the electric and magnetic intensities, respectively.

To accomplish the spatial discretization, the field components are arranged on the Yee grid [21] in the usual manner. Then, for each derivative that appears in the curl operators, central differences are invoked. For example, letting ψ represent a component of either \mathbf{E} or \mathbf{H} and letting δ_x be the length of the cell, we write at node i ,

$$\left. \frac{\partial \psi}{\partial x} \right|_i \approx \frac{\psi_{i+1/2} - \psi_{i-1/2}}{\delta_x} = L_2 \psi_i. \quad (61)$$

Here L_2 denotes the second-order order discrete difference operator. In like fashion,

$$\left. \frac{\partial \psi}{\partial x} \right|_i \approx \frac{9}{8} \left(\frac{\psi_{i+1/2} - \psi_{i-1/2}}{\delta_x} \right) - \left(\frac{\psi_{i+3/2} - \psi_{i-3/2}}{24\delta_x} \right) = L_4 \psi_i, \quad (62)$$

which is a fourth-order approximation. In this case, the fourth-order discrete difference operator is represented by L_4 . Sixth- and eighth-order approximations can be easily effected using standard Taylor analysis.

To verify the claim on accuracy order, let $\psi = \psi_0 e^{-jkx}$, where ψ_0 is a constant scalar. In accordance with Fourier theory, the transform of $\partial/\partial x$ is $-jk$, whereas the transforms of L_2 and L_4 are denoted as $-jK_2$ and $-jK_4$, respectively. Here,

$$K_2 = \frac{2}{\delta_x} \sin \left(\frac{k\delta_x}{2} \right) \quad (63)$$

and

$$K_4 = K_2(1 + \delta_x^2 K_2^2 / 24). \quad (64)$$

Now as $\delta_x \rightarrow 0$, it is a simple matter to show that $K_2 \rightarrow k + \mathcal{O}(\delta_x^2)$ and $K_4 \rightarrow k + \mathcal{O}(\delta_x^4)$, as expected.

Extending these concepts to the vector fields of Maxwell, we deduce that the Fourier transform of $\nabla \times$ is $-j\mathbf{k}$, where $\mathbf{k} = k_x \mathbf{a}_x + k_y \mathbf{a}_y + k_z \mathbf{a}_z$, and the Fourier transform of the discrete version of $\nabla \times$ is $-j\mathbf{K}_q$, where $q = 2$ or $q = 4$, depending upon the accuracy order. For example,

$$\mathbf{K}_2 = \frac{2}{\delta_x} \sin \left(\frac{k_x \delta_x}{2} \right) \mathbf{a}_x + \frac{2}{\delta_y} \sin \left(\frac{k_y \delta_y}{2} \right) \mathbf{a}_y + \frac{2}{\delta_z} \sin \left(\frac{k_z \delta_z}{2} \right) \mathbf{a}_z. \quad (65)$$

A similar representation for \mathbf{K}_4 is constructed using equations like Eqn. (64). Thus, as $\delta_x, \delta_y, \delta_z$ all uniformly go to zero, $\mathbf{K}_q \rightarrow \mathbf{k} + \mathcal{O}(\delta_x^q, \delta_y^q, \delta_z^q)$.

We now seek to develop an integrator based upon leap-frog concepts and the following expansions. At $t = n\delta_t$,

$$\mathbf{H}^{n+1/2} = \mathbf{H}^{n-1/2} + 2 \sum_{m=1}^M \frac{1}{m!} \left(\frac{\delta_t}{2}\right)^m \frac{\partial^m \mathbf{H}^n}{\partial t^m} \quad (66)$$

and at $t = (n + 1/2)\delta_t$,

$$\mathbf{E}^{n+1} = \mathbf{E}^n + 2 \sum_{m=1}^M \frac{1}{m!} \left(\frac{\delta_t}{2}\right)^m \frac{\partial^m \mathbf{E}^{n+1/2}}{\partial t^m}. \quad (67)$$

When $M = 1$, the popular second-order Yee scheme emerges. That is, replacing time derivatives with curl operators in accordance with Eqns. (59) and (60), we obtain

$$\mu \mathbf{H}^{n+1/2} = \mu \mathbf{H}^{n-1/2} - \delta_t \nabla \times \mathbf{E}^n \quad (68)$$

and

$$\epsilon \mathbf{E}^{n+1} = \epsilon \mathbf{E}^n + \delta_t \nabla \times \mathbf{H}^{n+1/2}. \quad (69)$$

When $M \neq 1$, high-order temporal derivatives of the field vectors must also be known. For a fourth-order approximation, Fang [22] converted third-order temporal derivatives into third-order spatial derivatives via repeated application of Maxwell's equations. For example,

$$\frac{\partial^3 \mathbf{E}}{\partial t^3} = - \left(\frac{c^2}{\epsilon}\right) \nabla \times \nabla \times \nabla \times \mathbf{H}, \quad (70)$$

where $c = 1/\sqrt{\mu\epsilon}$. As can be inferred from the previous expression, this conversion process leads to a computational algorithm of great complexity. For in this expression there exists mixed higher-order derivatives that are not compatible with the Yee grid or with the boundary conditions. Moreover, if one seeks to develop a sixth- or eighth-order integrator, the complexity of the algorithm increases even more dramatically. From a memory point of view, the algorithm does not require any additional temporary storage vectors. Hence, Fang chooses memory parsimony at the expense of algorithm complexity. Like Yee's original scheme, Fang's scheme requires a total of six unknowns per three-dimensional cell.

Instead of converting temporal derivatives into spatial derivatives, we choose to adopt an extended leap-frog methodology. For example, a fourth-order integrator is constructed as follows:

$$\begin{aligned} \mathbf{T}_1 &= -(\delta_t/\mu) \nabla \times \mathbf{E}^n \\ \mathbf{T}_2 &= (\delta_t/\epsilon) \nabla \times \mathbf{T}_1 \\ \mathbf{T}_3 &= -(\delta_t/\mu) \nabla \times \mathbf{T}_2 \\ \mathbf{H}^{n+1/2} &= \mathbf{H}^{n-1/2} + \mathbf{T}_1 + \mathbf{T}_3/24. \end{aligned} \quad (71)$$

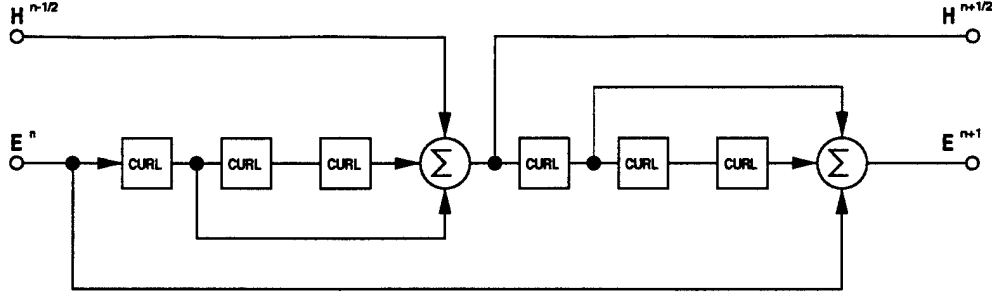


Figure 20: A pictorial representation of the extended fourth-order, leap-frog integrator (multiplicative constants omitted).

Here \mathbf{T}_1 , \mathbf{T}_2 and \mathbf{T}_3 are temporary storage vectors. To compute the curl operators, it is understood from the previous development that \mathbf{T}_1 is spatially proportional to \mathbf{H} ; hence, \mathbf{H} and \mathbf{T}_1 are spatially registered on the Yee grid. By way of similar comparison, \mathbf{E} and \mathbf{T}_2 are spatially registered, as are \mathbf{H} and \mathbf{T}_3 . Now for the next half time step,

$$\begin{aligned}\mathbf{T}_1 &= (\delta_t/\epsilon)\nabla \times \mathbf{H}^{n+1/2} \\ \mathbf{T}_2 &= -(\delta_t/\mu)\nabla \times \mathbf{T}_1 \\ \mathbf{T}_3 &= (\delta_t/\epsilon)\nabla \times \mathbf{T}_2 \\ \mathbf{E}^{n+1} &= \mathbf{E}^n + \mathbf{T}_1 + \mathbf{T}_3/24.\end{aligned}\tag{72}$$

Here the pairs $(\mathbf{T}_1, \mathbf{E})$, $(\mathbf{T}_2, \mathbf{H})$ and $(\mathbf{T}_3, \mathbf{E})$ are nodally collocated. A pictorial representation of the extended fourth-order leap-frog integrator is shown in Figure 20.

For the sake of simplicity, we have included the temporary vector \mathbf{T}_3 in the algorithm. However, in code it is not necessary since the calculations for \mathbf{T}_3 and \mathbf{E}^{n+1} (or \mathbf{T}_3 and $\mathbf{H}^{n+1/2}$) can be combined. Hence, the present approach requires twelve unknowns (i.e., three components of $\mathbf{E}, \mathbf{H}, \mathbf{T}_1$ and \mathbf{T}_2) per cell for a three-dimensional domain. Whereas for the four-stage Runge-Kutta (RK4) integrator, twelve to twenty-four unknowns per cell are needed, depending upon the approach [18]. (As storage requirements lessen for each of these RK4 procedures, the operational count or the algorithm complexity may increase.) Thus, it can be argued that the aforementioned leap-frog integrator expends additional memory (albeit, a small amount of additional memory) for the sake of algorithm simplicity. For we note that one could write two subroutines: one to compute the curl of \mathbf{E} and one to compute the curl of \mathbf{H} (the curl is computed to the level of spatial accuracy desired; more will be said on this in an ensuing discussion). In each of these subroutines, the appropriate boundary condition information is included. Then, to advance the equations, one needs only to repeatedly call each of these routines, one after the other, in accordance with the previous set of equations. At the end of each half-time step, the results are combined to obtain the next time-value of the vector under consideration.

Given the simplicity of the fourth-order algorithm, it requires little inductive reasoning to formulate the eighth-order extended leap-frog integrator. The final algorithm is

$$\mathbf{T}_1 = -(\delta_t/\mu)\nabla \times \mathbf{E}^n$$

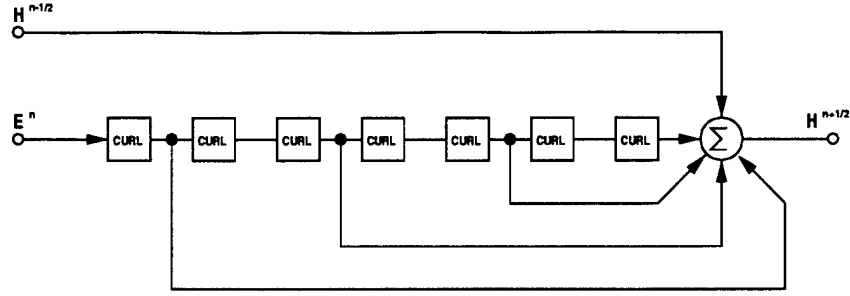


Figure 21: A pictorial representation of the extended eighth-order, leap-frog integrator (multiplicative constants omitted; only one stage is shown).

$$\begin{aligned}
 \mathbf{T}_2 &= (\delta_t/\epsilon) \nabla \times \mathbf{T}_1 \\
 \mathbf{T}_3 &= -(\delta_t/\mu) \nabla \times \mathbf{T}_2 \\
 \mathbf{T}_2 &= (\delta_t/\epsilon) \nabla \times \mathbf{T}_3 \\
 \mathbf{T}_5 &= -(\delta_t/\mu) \nabla \times \mathbf{T}_2 \\
 \mathbf{T}_2 &= (\delta_t/\epsilon) \nabla \times \mathbf{T}_5 \\
 \mathbf{T}_7 &= -(\delta_t/\mu) \nabla \times \mathbf{T}_2 \\
 \mathbf{H}^{n+1/2} &= \mathbf{H}^{n-1/2} + \mathbf{T}_1 + \mathbf{T}_3/24 + \mathbf{T}_5/1920 + \mathbf{T}_7/322560.
 \end{aligned} \tag{73}$$

In the same fashion,

$$\begin{aligned}
 \mathbf{T}_1 &= (\delta_t/\epsilon) \nabla \times \mathbf{H}^{n+1/2} \\
 \mathbf{T}_2 &= -(\delta_t/\mu) \nabla \times \mathbf{T}_1 \\
 \mathbf{T}_3 &= (\delta_t/\epsilon) \nabla \times \mathbf{T}_2 \\
 \mathbf{T}_2 &= -(\delta_t/\mu) \nabla \times \mathbf{T}_3 \\
 \mathbf{T}_5 &= (\delta_t/\epsilon) \nabla \times \mathbf{T}_2 \\
 \mathbf{T}_2 &= -(\delta_t/\mu) \nabla \times \mathbf{T}_5 \\
 \mathbf{T}_7 &= (\delta_t/\epsilon) \nabla \times \mathbf{T}_2 \\
 \mathbf{E}^{n+1} &= \mathbf{E}^n + \mathbf{T}_1 + \mathbf{T}_3/24 + \mathbf{T}_5/1920 + \mathbf{T}_7/322560.
 \end{aligned} \tag{74}$$

A pictorial representation for this integrator is shown in Figure 21. (Only one stage is shown.) Again, the temporary variable \mathbf{T}_7 is used to clarify the algorithmic procedure; in code it is not needed. Hence, for a three-dimensional domain, the eighth-order integrator requires 18 unknowns per cell (i.e., \mathbf{E} , \mathbf{H} , \mathbf{T}_1 , \mathbf{T}_2 , \mathbf{T}_3 and \mathbf{T}_5). In general, the M th-even-order leap-frog integrator requires $3M/2 + 6$ unknowns per cell for $M \geq 4$.

The complete numerical scheme is assembled by choosing the accuracy order for the temporal and spatial discretizations. Limiting ourselves to fourth-order accurate schemes or less, the following schemes will be considered: 2x2, 2x4, 4x2 and 4x4, where the first digit denotes the temporal accuracy and the second digit denotes the spatial accuracy. To ascertain the error mechanisms of these aforementioned schemes, a time-harmonic plane

wave is assumed for each of the field constituents. That is, let $\mathbf{E} = \mathbf{E}_0 e^{j\omega t} e^{-j\mathbf{k}\cdot\mathbf{x}}$ and $\mathbf{H} = \mathbf{H}_0 e^{j\omega t} e^{-j\mathbf{k}\cdot\mathbf{x}}$. Then for \mathbf{E} and \mathbf{H} to be solutions to the discretized Maxwell's equations, for an unbounded medium, we must require that

$$j\Omega\epsilon\mathbf{E}_0 = -j\mathbf{K}_q \times \mathbf{H}_0 - j\kappa_p(c^2\delta_t^2/24)\mathbf{K}_q \times [\mathbf{K}_q \times (\mathbf{K}_q \times \mathbf{H}_0)] \quad (75)$$

and

$$j\Omega\mu\mathbf{H}_0 = j\mathbf{K}_q \times \mathbf{E}_0 + j\kappa_p(c^2\delta_t^2/24)\mathbf{K}_q \times [\mathbf{K}_q \times (\mathbf{K}_q \times \mathbf{E}_0)], \quad (76)$$

where $q = 2$ for a spatially second-order accurate scheme (see Eqn. (65)) and $q = 4$ for a spatially fourth-order accurate scheme. Here κ_p is a switch whose value is zero for $p = 2$ (i.e., temporally second-order) and unity for $p = 4$ (temporally fourth-order). Moreover,

$$\Omega = \left(\frac{2}{\delta_t}\right) \sin\left(\frac{\omega\delta_t}{2}\right), \quad (77)$$

which reduces to ω as $\delta_t \rightarrow 0$. On the Cartesian grid, $\mathbf{K}_q \cdot \mathbf{E} = 0$ and $\mathbf{K}_q \cdot \mathbf{H} = 0$. Hence, Eqns. (75) and (76) reduce to

$$\Omega\epsilon\mathbf{E}_0 = -[1 - \kappa_p(c^2\delta_t^2/24)(\mathbf{K}_q \cdot \mathbf{K}_q)]\mathbf{K}_q \times \mathbf{H}_0 \quad (78)$$

and

$$\Omega\mu\mathbf{H}_0 = [1 - \kappa_p(c^2\delta_t^2/24)(\mathbf{K}_q \cdot \mathbf{K}_q)]\mathbf{K}_q \times \mathbf{E}_0. \quad (79)$$

Further manipulations of the previous equations results in the elimination of the field vectors. The final equation is given by

$$\Omega^2 = c^2\mathbf{K}_q \cdot \mathbf{K}_q[1 - \kappa_p(c^2\delta_t^2/24)(\mathbf{K}_q \cdot \mathbf{K}_q)]^2, \quad (80)$$

which is the numerical dispersion relationship for the pXq scheme. As the grid size and the time-step approach a value of zero, Eqn. (80) reduces to its analytical counterpart: $\omega^2 = c^2\mathbf{k} \cdot \mathbf{k}$.

Eqn. (80) contains the complete dispersion, dissipation and stability properties of the schemes. First consider the stability property. Fourier stability is assured if $\text{Im}\{\omega\} > 0$, where ω is a solution of Eqn. (80). Thus, seeking such solutions in a one-dimensional domain for which $\text{Im}\{\omega\} > 0$, one finds that δ_t must be less in value than $\nu\delta_x/c$, where ν is the maximum CFL number [23]. For three-dimensional domains, the requirement on δ_t is $\delta_t < \nu\delta_x/(\sqrt{3}c)$, provided the cells are cubic. Table 4 lists the maximum CFL values for each scheme. (These values have also been confirmed through experimental methods.) Although spatial accuracy does not have much impact on the CFL number, temporal accuracy does. From Table 4, we observe that the fourth-order in time schemes have a CFL number at least 2.4 times that of the second-order in time schemes. Moreover, the 4x4 scheme has a factor of 2.44 in CFL performance over Fang's scheme, which has a CFL of unity [24]. Even though the 4x4 scheme and Fang's scheme are based upon the same Taylor series expansion, they are not the same scheme. The 4x4 scheme uses exclusively fourth-order central differences to

Method	ν
2x2	1
2x4	6/7
4x2	2.847
4x4	2.441

Table 4: Maximum CFL number for each scheme.

calculate the first-order spatial derivatives; Fang's scheme uses a mixture of approximations for the various spatial derivatives of different orders that appear in the algorithm.

Provided that the time-step is selected to yield stable data, the dissipation and dispersion properties of each scheme can also be ascertained from Eqn. (80). First, it is easily confirmed that stable solutions of Eqn. (80) are purely real, thus implying that all four schemes are dissipationless. Second, the computed phase per time step of the signal ϕ_c is simply (for a one-dimensional domain),

$$\phi_c = 2 \sin^{-1} \left[\left(\frac{c\delta_t}{2} \right) \sqrt{K_q^2 [1 - \kappa_p (c^2 \delta_t^2 / 24) K_q^2]^2} \right], \quad (81)$$

whereas the exact phase of the signal, ϕ_e is $\omega\delta_t = \nu\delta_x k = 2\pi\nu/N_p$, where N_p is the number of cells per wavelength. By definition, the phase error, $\Delta\phi$, is $\phi_e - \phi_c$. A plot of $\Delta\phi$ is shown in Figure 22 as a function of N_p for the 2x2, 2x4, 4x2, 4x4 schemes, when $\nu = 0.5$. As expected, the 4x4 scheme has the best phase error characteristics. For example, for a phase error of .1 mr (i.e., phase error of 5.7 degrees after 1000 time steps), the 4x4 scheme requires $N_p = 12$; for the 2x2 scheme, $N_p = 33$. Another interesting feature of Figure 22 is the poor phase performance of the 4x2 scheme relative to the 2x2 scheme. Finally, the 2x4 is noted to be the only phase leading scheme.

Now that the phase characteristics are known, we can ascertain the overall efficiency of the 2x2 and the 4x4 schemes on a three-dimensional domain, sub-divided into cubic cells. The 2x2 scheme requires 30 computations per cell per time step and the 4x4 scheme requires 174 computations per cell per time step. Hence, for a computational domain of one wavelength on a side, a phase error of .1 mr per time step, a CFL of 0.5 and for a propagation distance of one wavelength along a major coordinate axis, the 2x2 scheme requires 71.2 million computations (i.e., $(30)(33)^4/ (.5)$) and .216 million memory units (i.e., $6(33)^3$); the 4x4 scheme requires only 7.22 million computations (i.e., $(174)(12)^4/ (.5)$) and 20.7 thousand memory units (i.e., $12(12)^3$). Thus, for this particular application, the 4x4 scheme is roughly ten times more efficient and requires ten times less memory than the 2x2 scheme. Although this example is idealized in many ways, the example substantiates the significant value of using the 4x4 scheme over the 2x2 scheme.

It is interesting to note that if $\nu = 1.3$ (near the 3D maximum value of the 4x4 scheme), the phase error analysis indicates that $N_p = 15$ is required for .1 mr of phase error per time step. Duplicating then the previous example, one finds that 6.77 million computations (i.e.,

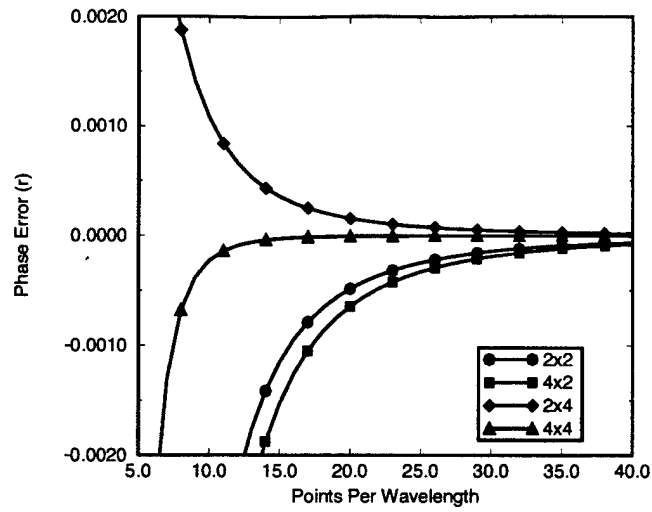


Figure 22: Phase error plots for various schemes: $\nu = 0.5$.

$(174)(15)^4/(1.3)$ and 40.5 thousand memory units (i.e., $12(15)^3$) are needed to propagate the signal one wavelength. Based upon this example, there appears to be no significant benefit to operating the 4x4 scheme at higher CFL.

References

- [1] D. M. Sheen, S. M. Ali, M. D. Abouzahra and J. A. Kong, "Application of the three-dimensional finite-difference time-domain method to the analysis of planar microstrip circuits," *IEEE Trans. Microwave Theory Tech.*, vol. 38, no. 7, pp. 849-857, 1990.
- [2] R. J. Luebbers and H. S. Langdon, "A simple feed model that reduces time steps needed for FDTD antenna and microstrip calculations," *IEEE Trans. Ant. Propagat.*, vol. 44, no. 7, pp. 1000-1005, 1996.
- [3] T. Shibata and H. Kimura, "Computer-aided engineering for microwave and millimeter-wave circuits using the FD-TD technique of field simulations," *Int'l J. of Microwave and Milli-meter Wave Computer-Aided Engineering*, vol 2., pp. 238-250, 1993.
- [4] B. Strand, "Summation by parts for finite difference approximations for d/dx ," *Journal of Computational Physics* vol. 110, 1994.
- [5] P. Olsson, "Summation by parts, projections, and stability. I," *Mathematics of Computation*, vol. 64, no. 211, 1995.
- [6] L. Zhao and A. C. Cangellaris, "GT-PML: Generalized theory of perfectly matched layers and its application to the reflectionless truncation of finite-difference time-domain grids," *IEEE Trans. Microwave Theory Tech.*, vol. 44, no. 12, 1996.
- [7] J. L. Young, D. Gaitonde, and J. S. Shang, "Towards the construction of a fourth-order difference scheme for transient wave simulation: Staggered grid approach," *IEEE Trans. Ant. Propagat.*, vol. 45, no. 11, pp. 1573-1580, 1997.
- [8] R. F. Harrington, *Time-Harmonic Electromagnetic Fields*, McGraw-Hill, New York, 1961.
- [9] D. Gaitonde, J. Shang and J. L. Young, "Practical aspects of higher-order numerical schemes for wave propagation phenomena," *Intl. J. Num. Methods in Engr.*, vol. 45, pp. 1849-1869.
- [10] D. A. Anderson, J. C. Tannehill and R. H. Pletcher, *Computational Fluid and Mechanics and Heat Transfer*, Taylor & Francis, Bristol, PA, 1984.
- [11] S. L. Ray, "Grid decoupling in finite element solutions of Maxwell's equations," *IEEE Trans. Ant. Propagat.*, vol. 40, no. 4, 1992.
- [12] J. S. Shang and D. Gaitonde, "Characteristic-based, time-dependent maxwell equation solvers on a general curvilinear frame," *AIAA Journal*, vol. 33, no. 3, pp. 491-498, 1995.
- [13] A. W. Al-Khafaji, *Numerical Methods in Engineering Practice*, Holt, Rinehart and Winstron, New York, 1986.

- [14] D. Gaitonde and J. S. Shang, "Optimized compact-difference-based finite-volume Schemes for linear wave phenomena," *J. Comp. Phys.*, vol. 138, pp. 617-643, 1997.
- [15] Gottlieb, D., and B. Yang, "Comparisons of staggered and non-staggered schemes for Maxwell's equations," *12 Annual Rev. of Progress in Appl. Comp. Electromagn.*, Monterey, CA, pp. 1122-1131, 1996.
- [16] Thomas, L. H., "Elliptic problems in linear difference equations over a network," *Watson Sci. Comput. Lab. Rept.*, Columbia University, New York, 1949.
- [17] Gustafsson, B., "The convergence rate for difference approximations to mixed initial boundary value problems," *Math. Comp.*, vol. 29, pp. 396-406, 1975.
- [18] Press, W. H., B. P. Flannery, S. A. Teukolsky, W. T. Vetterling, *Numerical Recipes*, Cambridge University Press, Cambridge, 1986.
- [19] Fyfe, D. J., "Economical evaluation of Runge-Kutta formulae," *Math. Comput.*, vol. 20, pp. 392-398, 1966.
- [20] Williamson, J. H., "Low-storage Runge-Kutta schemes," *J. Comp. Physics*, vol. 35, pp. 48-56, 1980.
- [21] K. S. Kunz and R. J. Luebbers, *The Finite Difference Time Domain Method for Electromagnetics*, CRC Press, Boca Raton, FL, 1993.
- [22] J. Fang, *Time Domain Finite Difference Computation for Maxwell's Equations*, Ph.D Dissertation, University of California, Berkeley, CA, 1989.
- [23] R. Richtmyer and K. Morton, *Difference Methods for Initial-Value Problems*, Wiley, New York, NY, 1967.
- [24] K. L. Shlager, J. G. Maloney, S. L. Ray, and A. F. Peterson, "Relative accuracy of several finite-difference time-domain methods in two and three-dimensions," *IEEE Trans. Ant. Propagat.*, vol. 41, no. 12, pp. 1732-1737, 1993.